

Rapid Microfluidic Dilution for Single-Molecule Spectroscopy of Low-Affinity Biomolecular Complexes

Niels Zijlstra, Fabian Dingfelder, Bengt Wunderlich, Franziska Zosel, Stephan Benke, Daniel Nettels, and Benjamin Schuler*

Abstract: To enable the investigation of low-affinity biomolecular complexes with confocal single-molecule spectroscopy, we have developed a microfluidic device that allows a concentrated sample to be diluted by up to five orders of magnitude within milliseconds, at the physical limit dictated by diffusion. We demonstrate the capabilities of the device by studying the dissociation kinetics and structural properties of low-affinity protein complexes using single-molecule two-color and three-color Förster resonance energy transfer (FRET). We show that the versatility of the device makes it suitable for studying complexes with dissociation constants from low nanomolar up to 10 μM , thus covering a wide range of biomolecular interactions. The design and precise fabrication of the devices ensure simple yet reliable operation and high reproducibility of the results.

Single-molecule spectroscopy has developed into a powerful approach for investigating biomolecular structure, dynamics, and interactions, especially in combination with Förster resonance energy transfer (FRET).^[1] However, a major challenge for studying the mechanisms of biomolecular interactions by single-molecule spectroscopy, such as FRET between two binding partners, is that their affinities are often so low that they rapidly dissociate at the about 10 to 100 pM sample concentrations required for single-molecule detection. As a result, single-molecule studies with two fluorescently labeled interaction partners are often not possible at equilibrium. This limitation can be circumvented by forming the complex at high concentrations, rapidly diluting the sample to single-molecule concentrations, and monitoring its properties before dissociation.^[2] However, there are currently no methods available that combine sufficiently large dilutions and short dead times to enable observation of such complexes before they dissociate. Herein, we demonstrate a solution to this problem using a microfluidic device that enables the sample to be diluted more than 10 000-fold within milliseconds and allows the properties of the complex and its

dissociation kinetics to be monitored by confocal single-molecule spectroscopy.

A suitable rapid dilution microfluidic device must meet several requirements. First, the dilution needs to be sufficiently rapid that even low-affinity complexes with high dissociation rates can be studied. The minimum time for dilution in laminar flow is fundamentally limited by translational diffusion. Given the diffraction-limited size of the confocal observation volume and the diffusion coefficient of typical biomolecular samples, the minimum dead time for a 10 000- to 100 000-fold dilution, for example, is in the range of a few milliseconds (Figure S1 in the Supporting Information). Second, since not all applications require the same dilution factor, the device must provide dilutions that can be adjusted over a wide range (about 1000- to 100 000-fold). Third, because high sample concentrations are required to form stable biomolecular complexes initially, the device should have a low sample consumption. Fourth, the accessible observation times should cover a range from milliseconds to minutes after dilution, so that dissociation kinetics can be monitored and quantified over a wide range of timescales (as required by different dissociation rates). Finally, for a quantitative analysis of the dissociation kinetics, it must be possible to accurately convert the positions throughout the device into times after dilution.^[3]

The layout of the microfluidic device is summarized in Figure 1 and the Supporting Information, Figures S2 and S3. Three inlet channels are merged for hydrodynamic focusing of the central sample stream by the two side buffer inlets.^[4] To achieve large dilutions, the majority of the sample is diverted to a shunt channel, while the tail of the concentration profile, corresponding to very low sample concentrations, is directed to the observation region (Figure 1c). In the subsequent broad observation region, the resulting steep concentration profile is expanded and then sectioned into several streams with different sample concentrations by a cascade of microfabricated wedges creating five outlet channels (Figure 1b). Figure 1a shows a concentration profile from 3D finite-element calculations of the dilution process. Different positions in the observation region and each of the four long-time observation channels provide access to different dilution factors and thus great flexibility in selecting positions along the streamlines with sample concentrations suited for single-molecule detection. Early positions in the observation region provide access to observation times milliseconds after dilution. With a total length of about 70 mm, each channel gives access to observation times of up to 3 minutes after dilution. Positions within the channels can be located accurately with the aid of position markers throughout the device.

[*] Dr. N. Zijlstra, F. Dingfelder, Dr. B. Wunderlich, Dr. F. Zosel, Dr. S. Benke, Dr. D. Nettels, Prof. Dr. B. Schuler
Department of Biochemistry, University of Zurich
Winterthurerstrasse 190, 8057 Zurich (Switzerland)
E-mail: schuler@bioc.uzh.ch

Prof. Dr. B. Schuler
Department of Physics, University of Zurich
Winterthurerstrasse 190, 8057 Zurich (Switzerland)

Supporting information and the ORCID identification number(s) for the author(s) of this article can be found under:
<https://doi.org/10.1002/anie.201702439>

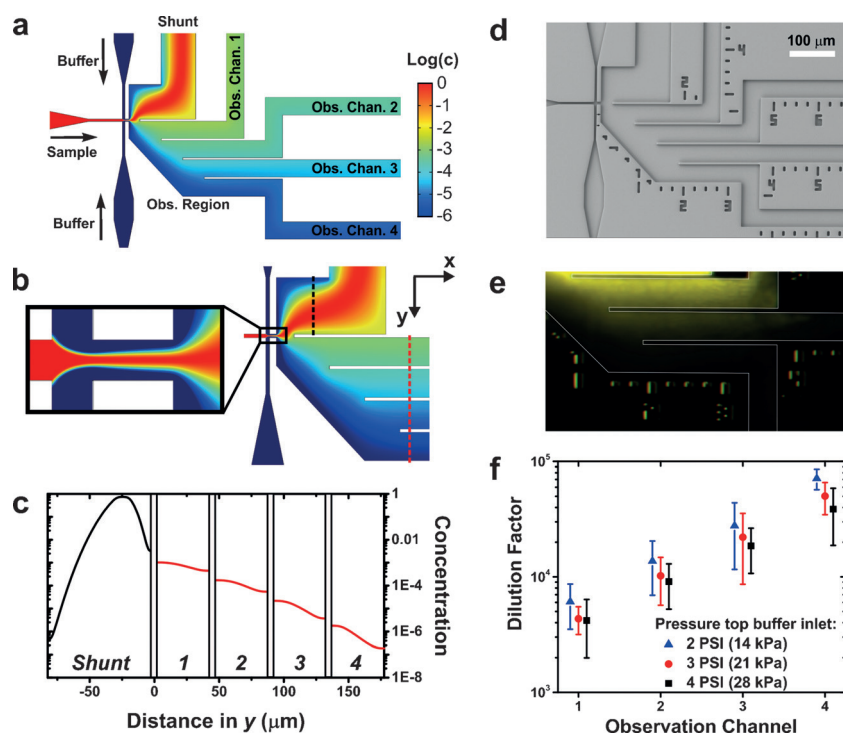


Figure 1. Design and characterization of the microfluidic rapid dilution device. a) Concentration profile based on 3D finite-element calculations of the dilution process. Hydrodynamic focusing of a concentrated sample (red) with buffer (dark blue) results in dilutions that span many orders of magnitude. Concentration is plotted on a logarithmic scale. b) Rapid dilution by concentration sectioning. Hydrodynamic focusing of the center sample stream by two side buffer inlets generates a sharp concentration gradient across a narrow channel [color scale as in (a)]. c) The tail of the concentration distribution is shaved off by the sectioning wedges and directed into the four observation channels. Black and red lines represent the cross sections of the concentration distribution in the y direction as indicated by the black and red dashed lines in (b), where $y=0$ is at the center of the top sectioning wedge. d) Scanning electron micrograph of the observation region and the cascade of wedges. e) Wide-field fluorescence image of the observation channels showing the dilution of 500 μM 20 kDa FITC-Dextran. f) Dilution factors for the four observation channels determined by FCS. Error bars are the standard deviation of three measurements in three separate microfluidic devices. The data points are offset horizontally for optimal visualization.

To attain sufficiently precise structures for accurate and reproducible measurements over a wide range of timescales, we employed precision microfabrication in silicon to generate device molds. Large numbers of devices can then be generated easily with high reproducibility by replica molding using polydimethylsiloxane (PDMS)^[5] (Figure 1d and the Supporting Information, Figure S3) and subsequent bonding to fused silica cover slides (see Supporting Information for details). Microfabricated filter arrays integrated in each inlet channel (Supporting Information, Figure S2) reduce complications from channel blockage; in combination with computer-controlled electro-pneumatic pressure controllers for driving fluid flow through the channels, stable operation of a single device can typically be maintained for several days.^[6] These improvements enable easy-to-use yet robust microfluidic devices for single-molecule experiments with highly reproducible results, as illustrated by the application of previous device designs produced and operated in this way.^[7]

The quality of the resulting rapid dilution microfluidic devices is confirmed by the agreement of the finite-element

calculations used in the design with the flow velocities measured throughout the microfluidic device with two-focus fluorescence correlation spectroscopy (FCS)^[8] (Supporting Information, Figures S4 and S5). Further, the sample concentrations in the microfluidic device were quantified using single-focus FCS. As shown in Figure 1f, the design indeed allows the sample to be diluted more than 10000-fold, thus enabling jumps from micromolar to subnanomolar concentrations. The concentration sectioning by the four different observation channels provides direct access to a broad range of different dilutions even at long times without changing the device. By adjusting the pressures applied to the center and side inlets, dilutions of up to 80000-fold can be achieved.

To benchmark the dead time and time resolution of the microfluidic device, we used single-molecule two-color FRET (2c-FRET) to follow the dissociation of a complex of two intrinsically disordered proteins (Figure 2a), the nuclear co-activator binding domain (NCBD) of the CREB binding protein and the activation domain (ACTR),^[9] which are involved in transcriptional regulation. The complex between donor- (Cy3B) and acceptor- (LD650^[10]) labeled ACTR and unlabeled NCBD was formed at protein concentrations of 1 μM , that is, far above the dissociation constant ($K_d = 10 \pm 3 \text{ nM}$), and loaded in the center sample inlet (a sample volume of 20 μL is sufficient to continuously measure for at least 8 hours). In the observation region, positions along the tail of the steep concentration profile were chosen where the sample reaches single-molecule concentrations (ca. 100 pM, that is, far below the K_d) to monitor the dissociation process (Figure 2b). For accurate extraction of the dissociation kinetics, we used a position-to-time conversion based on time-dependent 3D finite-element calculations (Supporting Information, Figure S6 and Video S1).^[3]

Figure 2b shows that FRET efficiency histograms can already be recorded $2.7 \pm 0.3 \text{ ms}$ after dilution. Further transfer efficiency histograms recorded at different positions in the observation region and along observation channel 2, corresponding to times after dilution ranging from $6.2 \pm 0.6 \text{ ms}$ to $66.5 \pm 3.3 \text{ s}$ (Figure 2b,c and the Supporting Information, Figure S7), show two relevant peaks: The high transfer-efficiency peak ($E = 0.79$) corresponds to the protein complex, and the peak at $E = 0.53$ to unbound ACTR. The histograms show that the fraction of complex decreases with increasing time after dilution, as expected. Structural properties, that is, the mean FRET efficiency, can already be extracted reliably at $2.7 \pm 0.3 \text{ ms}$ after dilution. However, the

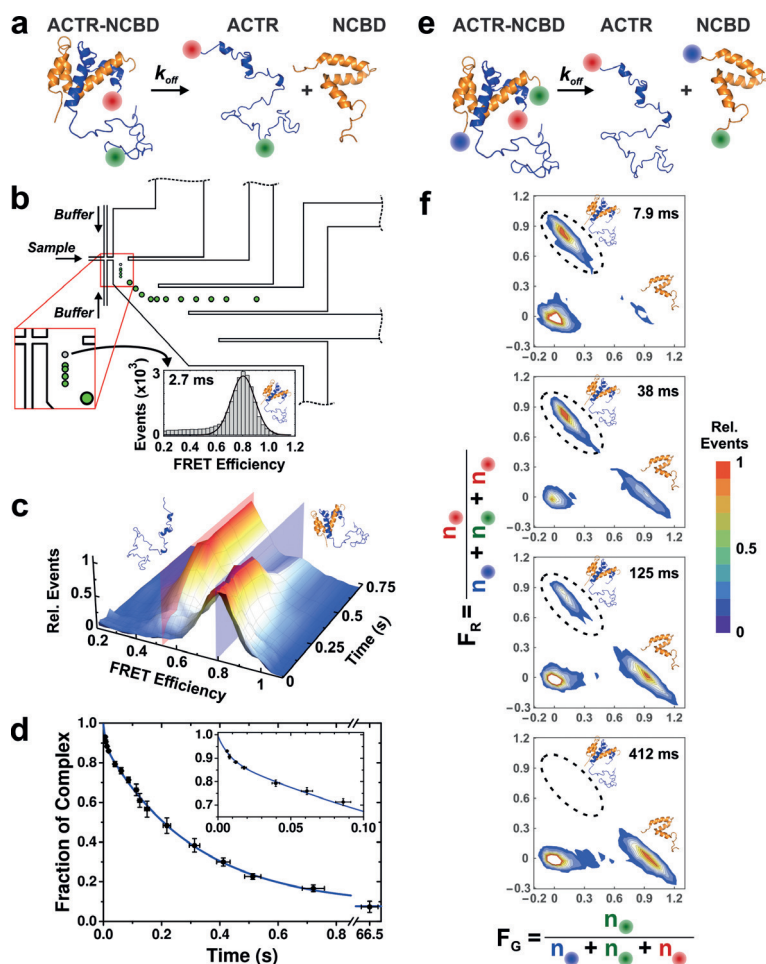


Figure 2. Dissociation kinetics and conformational properties of the ACTR-NCBD complex monitored by 2c- and 3c-FRET (a, e) in the rapid dilution device. b) Transfer efficiency histograms were recorded at 16 positions (green circles), each corresponding to a different time after dilution. c) Time series of 2c-FRET efficiency histograms showing that the peak amplitude corresponding to the complex ($E=0.79$, blue plane) decreases, while the peak amplitude for unbound ACTR ($E=0.53$, red plane) increases with time after dilution. Each histogram is normalized to its maximum value. d) Fraction of complex (black circles) determined from the fits to the transfer efficiency histograms as a function of time after dilution. Vertical error bars are the standard deviation from three independent measurements in separate microfluidic devices. Inset: Expansion of the initial 100 ms. Horizontal error bars were obtained assuming an uncertainty of $\pm 0.5 \mu\text{m}$ in detection position and flow velocity variations of $\pm 5\%$.^[6] Data were fitted with a double-exponential decay (solid blue line). f) Representative three-color 2D histograms of photon count ratios show that both intra- and intermolecular FRET in the ACTR-NCBD complex (indicated by the dashed ellipse) can be monitored before dissociation. Histograms are normalized to the maximum of the bound and unbound populations.

low number of photons per burst (resulting from the high flow velocities) and the relatively high sample concentration at these early times limit the accuracy with which absolute populations can be obtained from peak integrals. Both the flow velocity and the sample concentration continue to drop until approximately 5 ms after dilution, and histograms suitable for accurately determining relative populations can be recorded starting approximately 6 ms after dilution (Supporting Information, Figure S8), close to the dead time dictated by diffusion-limited dilution (Supporting Information, Figure S1).

To quantify the dissociation kinetics, the fraction of ACTR-NCBD complex was determined for each histogram from the ratio of the area of the high-efficiency peak and the total peak area. Figure 2d shows the results obtained from three independent measurements in three separate microfluidic devices (see the Supporting Information, Figure S11, for a comparison of the three datasets). The kinetics deviate from single-exponential behavior, as expected from previous work,^[11] and were thus fitted with a double-exponential function. The resulting rate constants, $k_{\text{off},1} = 3.2 \pm 0.1 \text{ s}^{-1}$ and $k_{\text{off},2} = 125 \pm 88 \text{ s}^{-1}$, are in good agreement with previously reported values.^[11a] Note that for the experimental conditions used here, with a ligand (NCBD) concentration of approximately $200 \mu\text{M}$ and a typical association rate constant on the order of $10^8 \text{ M}^{-1} \text{ s}^{-1}$, the contribution of the association rate to the observed rate is about 0.02 s^{-1} , and is therefore negligible in the observed dissociation kinetics. These results illustrate the fidelity and time resolution of this device. Kinetics are accessible down to the low millisecond range, making the device suitable even for probing protein complexes with low stability and correspondingly large dissociation rates. An example is shown in the Supporting Information, Figure S12, for a destabilized ACTR-NCBD complex with a dissociation constant K_d of approximately $8 \mu\text{M}$ and a corresponding dissociation rate of $k_{\text{off}} = 540 \pm 21 \text{ s}^{-1}$.

This rapid dilution device is thus enables the study of the structure of low-affinity biomolecular complexes that are inaccessible in equilibrium single-molecule measurements due to their rapid dissociation. Especially for intermolecular FRET experiments, in which both binding partners must be fluorescently labeled, rapid dilution of the preformed complex to single-molecule concentrations is required for intermolecular distances to be monitored before dissociation. We demonstrate this capability in three-color FRET (3c-FRET) measurements on the ACTR-NCBD complex ($K_d = 60 \pm 15 \text{ nm}$, Figure 2e). As in the 2c-FRET experiments, the preformed complex between donor- (Alexa Fluor 488) and acceptor- (Alexa Fluor 594) labeled NCBD and acceptor- (Biotium CF680R) labeled ACTR ($1 \mu\text{M}$) was loaded into the sample inlet. 2D histograms of photon count ratios reporting on intra- (F_G) and intermolecular FRET (F_R) were recorded at positions along the tail of the steep concentration profile where the sample reached single-molecule concentrations, corresponding to times after dilution between $7.9 \pm 0.8 \text{ ms}$ and $66.5 \pm 3.3 \text{ s}$ (Figure 2f and Figure S9, for details see Supporting Information). The 2D histograms (Figure 2f) show three peaks. The peak at ($F_G = 0.1$, $F_R = 0.85$) corresponds to the complex, the peak at ($F_G = 0.9$, $F_R = 0$) to unbound NCBD, and the peak at ($F_G = 0$, $F_R = 0$) to molecules lacking an active red or green acceptor dye.

With increasing time after dilution and corresponding dissociation, the fraction of complex decreases and the fraction of free NCBD increases, as expected. The dissociation kinetics (Supporting Information, Figure S10) exhibit a double exponential decay, with rate constants $k_{\text{off},1} = 4.3 \pm 0.4 \text{ s}^{-1}$ and $k_{\text{off},2} = 37 \pm 10 \text{ s}^{-1}$, which are close to those measured in the 2c-FRET experiments, with small differences presumably resulting from differences in labeling and buffer conditions. With its dissociation on a 100-ms timescale, the complex is clearly inaccessible to observation at single-molecule concentrations by manual dilution. In the rapid dilution device, however, it can be transiently populated, and intra- and intermolecular distance information can be obtained before dissociation occurs.

In summary, we present a novel microfluidic device for single-molecule spectroscopy that is capable of diluting a concentrated sample by almost five orders of magnitude in milliseconds. We show that this device can be used to transiently populate and study the structural properties of low-affinity complexes and to quantify the dynamics of the dissociation process over a wide range of timescales. The design and precision fabrication of the devices ensure simple yet reliable operation on a day-to-day basis and high reproducibility of the results. The versatility of the device in terms of accessible dilutions, long observation times, and short dead time makes it suitable for studying biomolecular complexes with dissociation times down to less than 10 ms. Assuming typical association rate constants of 10^5 – $10^7 \text{ M}^{-1} \text{ s}^{-1}$,^[12] this enables the study of complexes with dissociation constants from low nanomolar to greater than $10 \mu\text{M}$, covering a wide range of biomolecular interactions.^[12b,13]

Acknowledgements

We thank S. Blanchard for the kind gift of LD650 maleimide; D. Scheiwiler (Institute of Mechanical Systems, ETH Zürich) for help with the microfabrication; A. Schmid and S. Weidner for technical support; the Center for Microscopy and Image Analysis, University of Zürich, for assistance with scanning electron microscopy; J. Schöppe and A. Plückthun for the kind gift of a pAT222-pD expression vector; and H. Hofmann and K. Buholzer for providing an expression plasmid for ACTR and NCBD. This work was supported by the Swiss National Science Foundation, grant numbers 205321_149624 and 31003A_152839 (B.S.) and by a Postdoctoral Fellowship of the Forschungskredit of the University of Zurich, grant no. FK-16-049 (N.Z.).

Conflict of interest

The authors declare no conflict of interest.

Keywords: FRET · intrinsically disordered proteins · microfluidics · protein–protein interactions · single-molecule studies

How to cite: *Angew. Chem. Int. Ed.* **2017**, *56*, 7126–7129
Angew. Chem. **2017**, *129*, 7232–7235

- [1] a) C. Joo, H. Balci, Y. Ishitsuka, C. Buranachai, T. Ha, *Annu. Rev. Biochem.* **2008**, *77*, 51–76; b) Y. Gambin, A. A. Deniz, *Mol. Biosyst.* **2010**, *6*, 1540–1547; c) B. Schuler, H. Hofmann, *Curr. Opin. Struct. Biol.* **2013**, *23*, 36–47.
- [2] a) Y. Gambin, V. VanDelinder, A. C. M. Ferreón, E. A. Lemke, A. Groisman, A. A. Deniz, *Nat. Methods* **2011**, *8*, 239–241; b) M. H. Horrocks, L. Rajah, P. Jonsson, M. Kjaergaard, M. Vendruscolo, T. P. Knowles, D. Klenerman, *Anal. Chem.* **2013**, *85*, 6855–6859.
- [3] B. Wunderlich, D. Nettels, B. Schuler, *Lab Chip* **2014**, *14*, 219–228.
- [4] a) J. B. Knight, A. Vishwanath, J. P. Brody, R. H. Austin, *Phys. Rev. Lett.* **1998**, *80*, 3863–3866; b) S. H. Pfeil, C. E. Wickersham, A. Hoffmann, E. A. Lipman, *Rev. Sci. Instrum.* **2009**, *80*, 055105.
- [5] J. C. McDonald, G. M. Whitesides, *Acc. Chem. Res.* **2002**, *35*, 491–499.
- [6] B. Wunderlich, D. Nettels, S. Benke, J. Clark, S. Weidner, H. Hofmann, S. H. Pfeil, B. Schuler, *Nat. Protoc.* **2013**, *8*, 1459–1474.
- [7] a) S. Benke, D. Roderer, B. Wunderlich, D. Nettels, R. Glockshuber, B. Schuler, *Nat. Commun.* **2015**, *6*, 6198; b) R. Kellner, H. Hofmann, A. Barducci, B. Wunderlich, D. Nettels, B. Schuler, *Proc. Natl. Acad. Sci. USA* **2014**, *111*, 13355–13360; c) I. König, A. Zarrine-Afsar, M. Aznauryan, A. Soranno, B. Wunderlich, F. Dingfelder, J. C. Stüber, A. Plückthun, D. Nettels, B. Schuler, *Nat. Methods* **2015**, *12*, 773–779; d) A. Soranno, A. Holla, F. Dingfelder, D. Nettels, D. E. Makarov, B. Schuler, *Proc. Natl. Acad. Sci. USA* **2017**, *114*, E1833–E1839.
- [8] T. J. Arbour, J. Enderlein, *Lab Chip* **2010**, *10*, 1286–1292.
- [9] a) S. J. Demarest, M. Martinez-Yamout, J. Chung, H. Chen, W. Xu, H. J. Dyson, R. M. Evans, P. E. Wright, *Nature* **2002**, *415*, 549–553; b) M. Kjaergaard, K. Teilmann, F. M. Poulsen, *Proc. Natl. Acad. Sci. USA* **2010**, *107*, 12535–12540.
- [10] R. B. Altman, D. S. Terry, Z. Zhou, Q. Zheng, P. Geggier, R. A. Kolster, Y. Zhao, J. A. Javitch, J. D. Warren, S. C. Blanchard, *Nat. Methods* **2012**, *9*, 68–71.
- [11] a) J. Dogan, X. Mu, Å. Engström, P. Jemth, *Sci. Rep.* **2013**, *3*, 2076; b) J. Dogan, T. Schmidt, X. Mu, Å. Engström, P. Jemth, *J. Biol. Chem.* **2012**, *287*, 34316–34324.
- [12] a) G. Schreiber, G. Haran, H. X. Zhou, *Chem. Rev.* **2009**, *109*, 839–860; b) Y. Huang, Z. Liu, *J. Mol. Biol.* **2009**, *393*, 1143–1159.
- [13] S. L. Shammass, M. D. Crabtree, L. Dahal, B. I. M. Wicky, J. Clarke, *J. Biol. Chem.* **2016**, *291*, 6689–6695.

Manuscript received: March 7, 2017

Revised manuscript received: April 11, 2017

Version of record online: May 16, 2017

Supporting Information

Rapid Microfluidic Dilution for Single-Molecule Spectroscopy of Low-Affinity Biomolecular Complexes

*Niels Zijlstra, Fabian Dingfelder, Bengt Wunderlich, Franziska Zosel, Stephan Benke, Daniel Nettels, and Benjamin Schuler**

anie_201702439_sm_miscellaneous_information.pdf
anie_201702439_sm_Movie_1.avi

Materials and Methods

3D finite-element calculations

Stationary calculations

Finite-element calculations were performed using COMSOL Multiphysics 5.1. The COMSOL Multiphysics *Creeping Flow* module was used to calculate stationary flow velocities (Figure S5), and the *Transport of Diluted Species* module was used to calculate stationary concentration profiles (Figures 1a-c). Since the device is symmetric in height, only the bottom half of the device needed to be modeled, which reduces the number of mesh elements and hence the calculation time and required memory.

Meshing with rectangular cuboids was optimized throughout the geometry such that regions with steep concentration gradients had the finest mesh. Typically, the mesh size ranged from 25 nm in the region of concentration sectioning up to 250 μm in the long observation channels. The maximum number of mesh elements is limited by available random-access memory (RAM), 256 GB in our case.

However, an even finer mesh would have been required for calculating the stationary concentration profiles, since no full convergence of the calculated concentration profiles was achieved, leaving some uncertainty in the determination of dilution factors. As a result of this limited accuracy intrinsic of finite-element calculations of such extreme dilutions, absolute concentrations had to be determined experimentally (Figure 1). The stationary flow velocity calculations were, however, not influenced by a finer mesh and were therefore used to confirm the quality of the resulting devices. The excellent agreement of the finite-element calculations with the flow velocities measured throughout the microfluidic device with two-focus fluorescence correlation spectroscopy (FCS)^[1] confirmed the quality of the resulting devices (Figures S4 and S5).

All calculations were performed for the pressures used during the experiments: 0.5 PSI (3.5 kPa) to the sample inlet, 4 PSI (28 kPa) to the buffer side inlets, and -3 PSI (-21 kPa) to the outlets. Due to a strong dependence of the dilution factor on the diffusion coefficient of the biomolecules used in the calculations, dilution factors were calculated for a broad range of different diffusion coefficients (Figure S13).

Impulse-response calculations

3D time-dependent finite-element calculations were employed to obtain an accurate conversion of positions in the observation channels to times after dilution (Figure S6 and Supporting Video S1). The calculations were performed as described previously,^[2] where the

total time range (0 – 120 s) and time resolution (depending on the location in the device: 0.025 – 50 ms) was optimized for the current device design. Stationary flow velocities, calculated as described above, were used as input for the COMSOL *Transport of Diluted Species* module to calculate the impulse response, i.e. the propagation of a short pulse of sample molecules throughout the microfluidic device. The origin of the pulse was chosen to be at the very end of the center sample inlet, since this is the position where sample dilution starts. The pulse was Gaussian-shaped in time with a standard deviation of 0.1 ms and spatially uniform across the channel. The size of mesh elements ranged from 50 nm in the region of concentration sectioning up to 10 μm in the observation channels.

Due to the effect of Taylor dispersion, the distribution of arrival times at a given position x in the observation channels is broadened.^[2-3] We determined from the propagating sample pulse, $c(t, x)$, both the mean arrival time, $\langle t \rangle(x)$, and the relative

uncertainty, $\sigma_{rel}(x) = \sqrt{\langle t^2 \rangle - \langle t \rangle^2} / \langle t \rangle$ (Figure S6b and c). Here we used $\langle t^n \rangle \equiv \int t^n c(t, x) dt / \int c(t, x) dt$, where $n = 1$ or 2 .

Production, characterization, and usage of the microfluidic devices

Fabrication of the silicon master for replica molding

A 4-inch diameter silicon master was used for replica molding with polydimethylsiloxane (PDMS). The silicon master was produced as described previously using photolithography and reactive ion etching.^[4] The chrome mask used for lithography (Compugraphics Jena, Germany) contained seven identical patterns for the microfluidic chips, each 25 mm x 25 mm in size (the drawing that can be used for the mask is provided in Supporting File 2; it can be viewed using the free software KLayout). To promote the adhesion of the photoresist to the silicon wafer, the wafer was exposed to hexamethyldisilazane (HMDS) for 30 s. A 1 μm -thick layer of negative photoresist (ma-N 1410, micro resist technology GmbH) was spin-coated on the wafer and soft-baked on a hot plate by slowly heating the wafer up from room temperature to a final temperature of 393 K and subsequently leave it for 90 s at the final temperature. A mask aligner (MA6/MB6, Süss) was used to expose the coated silicon wafer to UV light (energy density: 450 mJ/cm² at 365 nm). Non-crosslinked photoresist was removed by gently applying a resist developer (ma-D533/S, micro resist technology GmbH) for 10 - 15 s.

Subsequently, 10 μm -deep structures were etched using a 3-step Bosch deep reactive-ion etching process (Estrelas 100, Oxford Instruments). Residual photoresist was

removed by placing the wafer in a plasma asher (300 E, TePla) for 5 min. The etching depth was verified using white-light interferometry (NewView 5000, Zygo).

Replica molding, assembly, and usage of the microfluidic devices

Replica molding and assembly of the microfluidic device was carried out as described previously.^[4] Briefly, the two components (silicone rubber compound and curing agent) of a PDMS kit (RTV615 A+B, Momentive Performance Materials) were mixed in a 10:1 ratio, stirred thoroughly, and degassed in a vacuum desiccator to remove air bubbles. To reduce the adhesion of PDMS to the silicon wafer, the wafer was exposed to trichloromethylsilane (TCMS) for ~30 min before it was mounted in a custom-made casting dish.^[4] Subsequently, the PDMS was poured into the casting dish and cured overnight at 60 °C.

After curing, individual device casts were excised from the PDMS replica using a scalpel and bonded to a clean 25 x 25 mm² glass cover slide (Corning) immediately after plasma activation (FEMTO plasma cleaner, Diener) and left overnight for optimal bonding. Subsequently, the microfluidic device was mounted in a custom-built cartridge system^[4] and loaded in a cartridge holder, which was mounted on the confocal microscope. Applying vacuum to the cartridge ensured tight adhesion between the PDMS device and the cartridge. Flow of solutions through the microchannels was achieved by applying pressured air to the inlets and by applying negative pressure to the outlets. Pressures were regulated by electro-pneumatic pressure controllers (T3110, Marsh Bellofram) connected to National Instruments I/O cards (NI 9201 and NI 9264 in combination with the NI cDAQ-9174 chassis). A custom-written Labview (National Instruments) program was used to set, read, and record the pressures. Before each measurement, the applied pressures were verified using a digital manometer.

Passivation of microfluidic devices

To reduce surface adhesion of sample proteins to the channel walls, the microchannels were passivated prior to each experiment by flushing an aqueous buffer solution (50 mM sodium phosphate, pH 7.0) containing 0.1 mg/ml poly(L-lysine)-*graft*-poly(ethylene glycol) (PLL-PEG) (PLL(20)-g[3.5]-PEG(2), Susos) through all microchannels for at least 1 h and subsequently flushing the microchannels with the same buffer solution to be used for the measurements for at least 20 min. The pressures applied to the microfluidic device during passivation were 2 PSI (14 kPa) to the sample and buffer inlets and -1.5 PSI (-10 kPa) to the outlets.

Scanning electron microscopy

Scanning electron microscopy (SEM) imaging of the microfluidic devices was carried out on a Zeiss SUPRA 50 VP microscope at the Center for Microscopy and Image Analysis (University of Zurich). A 5-10 nm layer of platinum was sputtered on the PDMS device casts in a high-vacuum coating unit (CCU-010, Safematic). SEM micrographs were used to verify the dimensions of the channels and to confirm the quality of the microstructures (Figure S3), showing that the structures can be fabricated with an accuracy of $\pm 5\%$.

Protein expression, purification, and labeling

ACTR

The coding sequence of a double-cysteine ACTR mutant was cloned via BamHI/HindIII into a pAT222-pD expression vector (gift of J. Schöppe and A. Plückthun^[5]), yielding an expression construct with an N-terminal Avi tag and a thrombin-cleavable C-terminal His6 tag:

MAGLNDIFEA QKIEWHEGSM GSGSGPCGTQ NRPLLNSLD DLVGPPSNLE GQSDERALLD
QLHTLLSNTD ATGLEEIDRA LGIPELVNQ GQALEPKQDC GGPRGSRQA SHHHHHH. pBirAcm (Avidity) was co-transfected for *in vivo* biotinylation of Lys12 in the Avi tag and expression was carried out in *E.coli* BL21(DE3) as described previously.^[6] The harvested cells were lysed by sonication and the His-tagged protein was enriched via immobilized metal affinity chromatography (IMAC) on a Ni-IDA resin (ABT). The His6 tag was then cleaved off with thrombin (Serva Electrophoresis) and separated from the protein via IMAC. Finally, biotinylated protein was separated from impurities and non-biotinylated protein via reverse-phase (RP) HPLC on a Reprosil Gold 200C18 column (Dr. Maisch) with a H₂O/0.1%TFA-acetonitrile gradient.

For labeling with the FRET dye pair, ACTR was dissolved under nitrogen atmosphere to a concentration of 200 μ M in 100 mM potassium phosphate buffer, pH 7.2 (labeling buffer). The protein was then first incubated for 3 hours at room temperature with a 0.8-fold molar ratio of Cy3B maleimide (GE Healthcare) to protein. Labeled protein was separated from unlabeled protein with RP-HPLC on a Sunfire C18 column (Waters) as described above. The appropriate fraction was lyophilized, re-dissolved in labeling buffer, and subsequently labeled with an 0.8-fold molar ratio of LD650 maleimide^[7] (Lumidyne Technologies) to protein. Double-labeled protein was separated from free dye on a Reprosil Gold 200 column and subjected to RP-HPLC on a Sunfire C18 column as a final purification step. The correct mass of labeled ACTR was confirmed by electrospray ionization mass spectrometry (ESI-MS). Using the same protocol, another sample of ACTR was labeled with two Atto 532 dyes with an equimolar

ratio of dye. Double-labeled protein was separated from single-labeled and unlabeled protein on a Reprosil Gold 200 column.

The single-cysteine ACTR construct used in the 3c-FRET experiments was co-expressed with NCBD from a pET-47b(+)vector.^[8] The expression construct contained an N-terminal His6 tag cleavable with HRV 3C protease, with the final amino acid sequence MAHHHHHSA ALEVLFGGPG TQNRPLLNS LDDLGGPSN LEGQSDERAL LDQLHTLLSN TDATGLEEIDRA LGIPELVNQG QALEPKQDC. Cell lysis and protein enrichment via IMAC were carried out as described above, followed by enzymatic cleavage of the His6 tag with HRV 3C protease and separation of the tag from the protein via IMAC. Finally, ACTR and NCBD were separated with RP-HPLC on a Reprosil Gold 200 column with a H₂O/0.1% TFA-acetonitrile gradient.

The single cysteine of the construct was labeled under the same conditions as described above, with an equimolar ratio of Biotium CF680R dye, followed by purification on a Reprosil Gold 200 column. The correct mass of the labeled protein was confirmed by ESI-MS.

NCBD

NCBD constructs were co-expressed with ACTR from a pET-47b(+) vector.^[8] The expression construct contained an N-terminal His6 tag cleavable with HRV 3C protease, yielding the final sequence used in the 2c-FRET experiments (MAHHHHHSA ALEVLFGGPC PNRSISPSAL QDLLRTLKSP SSPQQQQQVL NILKSNPQLM AAFIKQRTAK YVANQPGMQ) and the double cysteine variant used in the 3c-FRET experiments (MAHHHHHSA ALEVLFGGPC PNRSISPSAL QDLLRTLKSP SSPQQQQQVL NILKSNPQLM AAFIKQRTAK YVANQPGMQC). Cell lysis and protein enrichment via IMAC were carried out as described for ACTR, followed by enzymatic cleavage of the His6 tag with HRV 3C protease and separation of the tag from the protein via another round of IMAC. Finally, ACTR and NCBD were separated with RP-HPLC as described above. The double-cysteine variant was sequentially labeled with Alexa Fluor 488 and Alexa Fluor 594 as described for ACTR above, with all purification steps carried out on a Reprosil Gold 200 column. The correct mass of double-labeled NCBD was confirmed by ESI-MS.

Experimental characterization of the microfluidic device

Quantifying concentrations by fluorescence correlation spectroscopy

To quantify the sample concentrations throughout the microfluidic device, single-focus fluorescence correlation spectroscopy (FCS) measurements were performed. The amplitude of the correlation function is inversely proportional to the average number of fluorescent particles in the confocal volume, which can be converted to a concentration.

FCS measurements were performed on a custom-built confocal microscope. Excitation light at 532 nm was provided by a continuous-wave solid-state laser (Laser Boxx, Oxxius) and coupled into the microscope objective (UplanApo 60/1.20W, Olympus) via a triple-band dichroic mirror (zt405/530/630rpc, Chroma Technology) at a power of 25 μ W (measured at the fully illuminated back aperture of the objective). Fluorescence light was collected through the same microscope objective, focused onto a 100 μ m pinhole, and then separated into two channels with a polarizing beam splitter. Fluorescence emission was additionally filtered by a bandpass filter (ET585/65M, Chroma Technology) before being focused onto single-photon avalanche detectors (τ -SPAD50, PicoQuant), which were connected to a HydraHarp 400 counting module (PicoQuant).

All measurements were done in 50 mM sodium phosphate buffer containing 0.001% (w/v) Tween-20 (pH 7.0). The ACTR concentration in the sample inlet was 10 μ M (doubly labeled with Atto 532); the side inlets were filled with buffer only. The laser focus was placed at defined positions inside the observation channels, and the fluorescence signal was recorded for 10 minutes at each position. The pressures applied to the microfluidic device were 0.5 PSI (3.5 kPa) to the sample inlet, 4 PSI (28 kPa) to the buffer side inlets, and -3 PSI (-21 kPa) to the outlets.

The donor fluorescence intensity cross-correlation curves (i.e. the two different polarizations were correlated) were fitted with the model for laminar flow and diffusion of Magde *et al.*,^[9] which assumes a 3D Gaussian-shaped confocal volume, with an additional triplet-state component:

$$G(\tau) = 1 + \frac{1}{N} \left[\left(1 + \frac{\tau}{\tau_D} \right) \sqrt{1 + s^2 \frac{\tau}{\tau_D}} \right]^{-1} \left[1 + f_T \exp\left(-\frac{\tau}{\tau_T}\right) \right] \exp\left[-\left(\frac{\tau}{\tau_{Flow}} \right)^2 \frac{1}{(1 + \tau/\tau_D)} \right],$$

where N is the mean number of particles in the confocal volume, τ_D is the translational diffusion time, s is the ratio of the transverse and longitudinal radii of the confocal volume, f_T

is the amplitude of the triplet component, τ_T is the triplet decay time, and τ_{Flow} is the lateral flow time through the confocal volume. τ_D was constrained to the value observed in the absence of flow in a separate stationary measurement. N was converted to a concentration using a calibration curve (Figure S14) obtained from FCS measurements with known sample concentrations ranging from 0.1 to 10 nM.

Determining flow velocities with two-focus FCS

Flow velocities in the microfluidic devices were determined using two-focus FCS^[1] as described previously.^[2] A solution with ~ 0.7 nM Alexa Fluor 488 (50 mM sodium phosphate, pH 7.0) was loaded both in the sample inlet and the side buffer inlets. The laser foci were placed at defined positions inside the observation channel, and the fluorescence signal was recorded for three minutes at each position. The pressures applied to the microfluidic device were 0.5 PSI (3.5 kPa) to the sample inlet, 4 PSI (28 kPa) to the buffer side inlets, and 3 PSI (-21 kPa) to the outlets. Examples of two-focus FCS data are shown in Figure S4.

Widefield fluorescence imaging

Widefield fluorescence imaging was performed on a custom-built instrument equipped with a 488 nm solid-state laser (Sapphire 488-100, Coherent). The laser light (~ 8 mW) was focused onto the back aperture of a microscope objective (Plan, 20x/0.40, Olympus) via a dichroic mirror (488 nm, Semrock). After passing an emission bandpass filter (HQ525/50, Chroma Technology), the fluorescence emission was imaged onto an EM-CCD camera (Ixon 87 BI, Andor).

The sample inlet of the microfluidic device was filled with 500 μ M FITC-Dextran 20 kDa (FD20S, Sigma Aldrich) in 50 mM sodium phosphate, pH 8.0, and the buffer inlets were filled with buffer solution (50 mM sodium phosphate, pH 8.0). The applied pressures were 0.5 PSI (3.5 kPa) to the sample inlet, 2 PSI (14 kPa) to the buffer side inlets, and -3 PSI (-21 kPa) to the outlets (Figure 1e).

Single-molecule instrumentation, measurement procedures and data analysis

Single-molecule 2c-FRET measurements

Single-molecule 2c-FRET measurements were performed at 295 K on the same custom-built instrument on which the (one focus) FCS measurements were done. The laser excitation power (532 nm, continuous-wave) was 50 to 75 μW (measured at the back aperture of the objective). After the polarizing beam splitter, each polarization component of the fluorescence light was further split onto a pair of donor-acceptor fluorescence detection channels using dichroic mirrors (635DCXR, Chroma Technology). Donor fluorescence emission was filtered by bandpass filters (ET585/65M, Chroma Technology) and focused on τ -SPAD50 (PicoQuant) single photon avalanche detectors (SPADs). Likewise, acceptor fluorescence emission was filtered by a longpass filter (RazorEdge LP647RU, Semrock) and focused on SPCM-AQR-13 (PerkinElmer Optoelectronics) SPADs. Photon arrival times were recorded by four channels of a HydraHarp 400 counting module (PicoQuant). To remove photon bursts originating from molecules lacking an active acceptor dye, the sample molecules were probed periodically with 635 nm pulses from a diode laser (LDH-D-C-635M, PicoQuant) operating at 5 MHz and a power of 25-35 μW (measured at the back aperture of the objective). The technique is similar to pulsed interleaved excitation (PIE),^[10] where both lasers are pulsed, but leads to higher emission rates and less photobleaching for the samples used here.

All measurements were done in 50 mM sodium phosphate buffer containing 1 mM β -mercaptoethanol and 0.01% (w/v) Tween-20 (pH 7.0). Starting concentrations in the sample inlet were 1 μM ACTR (donor- (Cy3B) and acceptor- (LD650) labeled) and 1.75 μM NCBD (unlabeled), resulting in $\sim 99\%$ of ACTR bound ($K_d = 10 \pm 3$ nM); the side inlets were filled with the buffer alone (50 mM sodium phosphate buffer containing 1 mM β -mercaptoethanol and 0.01% (w/v) Tween-20 (pH 7.0)).

The measurements for the destabilized ACTR-NCBD complex were done in 50 mM sodium phosphate buffer containing 1 mM β -mercaptoethanol, 0.01% (w/v) Tween-20, and 3M Urea (pH 7.0). Starting concentrations in the sample inlet were 1 μM ACTR (donor- (Cy3B) and acceptor- (LD650) labeled) and 12.5 μM NCBD (unlabeled), resulting in $\sim 60\%$ of ACTR bound ($K_d = 8 \pm 1$ μM); the side inlets were filled with buffer only (50 mM sodium phosphate buffer containing 1 mM β -mercaptoethanol, 0.01% (w/v) Tween-20, and 3M Urea (pH 7.0)).

The pressures applied to the microfluidic device were 0.5 PSI (3.5 kPa) to the sample inlet, 4 PSI (28 kPa) to the buffer side inlets, and -3 PSI (-21 kPa) to the outlets.

Single-molecule 2c-FRET data analysis

Photon time series were first time-gated to select the emission resulting from the donor and direct acceptor excitation, respectively. Emission after donor excitation was corrected for the different quantum yields of the dyes, different detection efficiencies, cross-talk, acceptor direct excitation, and background. Fluorescence bursts from individual molecules were identified^[11] by combining successive photons separated by less than 50 μ s and bursts retained as an event if the total number of photons detected was greater than a threshold of 40 – 60, depending on the flow velocity at the specific location in the microfluidic device (i.e., the higher the flow velocity, the lower the residence time of the molecule in the confocal volume and hence the lower the number of photons collected per burst). To exclude acceptor dye bleaching events, the difference in the mean arrival times of the photons in the donor and acceptor channel was histogrammed and only bursts within a band of one standard deviation around the mean were used.^[12]

From the identified photon bursts we selected only those which also showed emission after direct acceptor excitation, with a stoichiometry ratio^[13] (S) of less than 0.7, where S is defined as $S = n_{Dex}/(n_{Dex} + \gamma n_{Aex})$, with n_{Dex} being the total number of photons after donor excitation, n_{Aex} the total number of photons after direct acceptor excitation, and γ a factor chosen such that the main FRET population is at $S = 0.5$. Typical intensity time traces and the identified fluorescence bursts are shown in Supporting Figure S15.

The resulting bursts were binned in a histogram according to their transfer efficiency (E), calculated for each selected burst from the number of photons from the corrected donor (n_D) and acceptor photon counts (n_A) after donor excitation according to $E = n_A/(n_A + n_D)$. The transfer efficiency histograms were fitted globally with a two-population model, where the populations were represented as Gaussian peaks (Figure S7). Global fit parameters were the positions of the two peaks; the amplitudes were fitted individually, and widths were fixed to 0.09. For each histogram, the fraction of bound ACTR was determined from the ratio of the area of the high-efficiency peak and the total peak area (Figure 2d).

Single-molecule 3c-FRET measurements

Single-molecule 3c-FRET measurements were performed at 295 K on the same custom-built instrument on which the 2c-FRET measurements were done, with a few adaptations. Excitation light was provided by a diode laser at 485 nm (LDH-D-C-485, PicoQuant) and coupled into the microscope objective (UplanApo 60/1.20W, Olympus) via a triple band dichroic mirror (BrightLine Di01-R488/543/635, Semrock) at a power of 100 μ W (measured at

the back aperture of the objective). Fluorescence light was collected by the same objective, focused onto a 100 μm pinhole, and separated into three channels with two consecutive dichroic mirrors (zt532RDC (Chroma) and T635lpxr (Chroma)). Fluorescence emission was collected by avalanche photodiode detectors after additional bandpass filtering (520/15 nm (BrightLine FF01-520/15, Semrock) and τ -SPAD50 (PicoQuant) for the donor channel, 615/20 nm (BrightLine FF01-615/20, Semrock) and τ -SPAD50 for the first acceptor channel, and 732/68 nm (BrightLine FF01-732/68, Semrock) and SPCM-AQR-13 (PerkinElmer Optoelectronics) for the second acceptor channel). The photon arrival times were recorded by three channels of a HydraHarp 400 counting module (PicoQuant).

All measurements were done in 50 mM sodium phosphate buffer containing 143 mM β -mercaptoethanol, 0.01% (w/v) Tween-20, and 1 M Trimethylamine *N*-oxide (TMAO) (pH 7.0). Protein concentrations in the sample inlet were 1 μM NCBD (donor- (Alexa Fluor 488) and acceptor- (Alexa Fluor 594) labeled) and 1 μM ACTR (labeled with CF680R) in buffer (50 mM sodium phosphate buffer containing 143 mM β -mercaptoethanol, 0.01% (w/v) Tween-20, and 1.16 M TMAO (pH 7.0)), resulting in about $\sim 94\%$ of NCBD bound ($K_d = 60 \pm 15$ nM). The side inlets were filled with only the buffer. The pressures applied to the microfluidic device were 0.5 PSI (3.5 kPa) to the sample inlet, 4 PSI (28 kPa) to the buffer side inlets, and -3 PSI (-21 kPa) to the outlets.

Single-molecule 3c-FRET data analysis

Detected photon counts were corrected for background, differences in quantum yields of the dyes, different detection efficiencies, crosstalk, and acceptor direct excitation. Fluorescence bursts were identified^[11] by combining successive photons separated by interphoton times of less than 100 μs and retained as a burst if the total number of photons detected was greater than a threshold of 40 – 50, depending on the flow velocity at the specific location in the microfluidic device. To exclude acceptor dye bleaching events, the difference in the mean arrival times of the photons in the donor and acceptor channel was histogrammed and only bursts within a band of 0.15 – 0.2 ms around the mean were used.^[12] This selection criterion was used for both the donor (Alexa Fluor 488) and first acceptor (Alexa Fluor 594), and for the first acceptor and second acceptor (CF680R).

The photon count ratios (PCRs) of the selected bursts were binned in a 2D histogram showing the fraction of detected photons from the first acceptor ($n_{594} / n_{488} + n_{594} + n_{680}$) versus the fraction of detected photons from the second acceptor ($n_{680} / n_{488} + n_{594} + n_{680}$) (Figure 1f and Figure S9). The 2D PCR histograms were fitted with three 2D Gaussian peak functions, one

for each of the three populations (donor only, unbound NCBD, and the NCBD-ACTR complex) (Figure S9). Since at short and long observation times, respectively, only two peaks are present (at short times, there is no unbound NCBD, and at long times no NCBD-ACTR complex), the peak positions and widths of the unbound NCBD and NCBD-ACTR complex were fixed based on free fits of the data obtained at intermediate observation times, where all three peaks were visible (9 out of 15 histograms). For each histogram, the fraction of NCBD-ACTR complex was determined from the ratio of the volume under the NCBD-ACTR complex peak and the volume under the unbound NCBD peak and NCBD-ACTR complex peak combined (Figure S10).

Figure S1: Diffusion-limited dilution

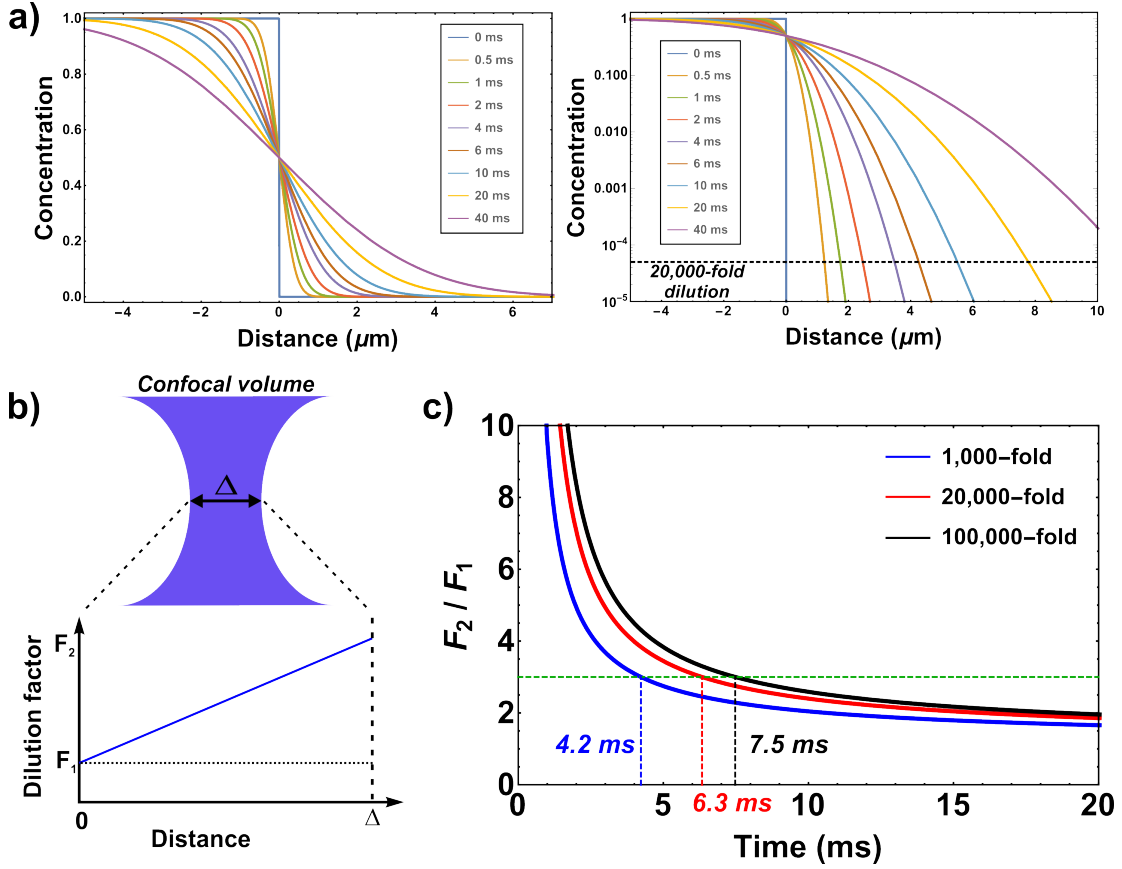


Figure S1: The fastest diffusion-driven dilution occurs next to a sharp concentration gradient. The time evolution of an initial concentration profile described by a step function is given by:

$$c(x, t) = \frac{c_0}{\sqrt{4\pi Dt}} \int_{-\infty}^0 \exp\left(\frac{-(x-x_0)^2}{4Dt}\right) dx_0 = \frac{c_0}{2} \left(1 - \operatorname{erf}\left(\frac{x}{\sqrt{4Dt}}\right)\right),$$

where c_0 is the starting concentration, D is the diffusion coefficient, x is the distance, t is the time, and erf is the error function. The time evolution is illustrated in **(a)**, assuming a diffusion coefficient of $D = 10^{-10} \text{ m}^2/\text{s}$ and $c_0 = 1$. The difference between left and right is the linear and logarithmic scale on the y-axis, respectively. The dilution factor is then given by $f(x, t) = c_0 / c(x, t)$. In principle, any dilution factor F can be found after arbitrarily short times at position $x_F(t) = \sqrt{4Dt} \operatorname{erf}^{-1}(1 - 2/F)$, where erf^{-1} is the inverse error function. In practice, however, if t is too small, the change in $f(x, t)$ across the dimensions of the confocal volume **(b)** is very high. Therefore, even if the dilution factor results in single-molecule concentrations at the center of the confocal observation volume, the signal is still dominated by the much higher concentrations within other regions of the observation volume that prevent the recording of signal from individual molecules.

The ratio of the dilution factors at opposite sides of the confocal volume, given by $\alpha(t) = F_2/F_1 = f(x_F(t) + \Delta/2, t) / f(x_F(t) - \Delta/2, t)$, is plotted as a function of time in **(c)**

for dilution factors F of 1,000, 20,000, and 100,000 (blue, red, and black lines, respectively) at the center of the confocal volume, assuming $\Delta = 300$ nm for the lateral width of the confocal volume. If we allow the variation of dilution across the focus to be at most $\alpha = 3$ (green dashed line in **(c)**), i.e., the dilution factor ranges from 10,000 – 30,000 over the dimensions of the confocal volume, $t = 6.3$ ms (red dashed line). Similarly, for a lower dilution of $F = 1,000$ at the center of the confocal volume, t decreases to 4.2 ms (blue dashed line), while for a higher dilution of $F = 100,000$ at the center of the confocal volume, t increases to 7.5 ms (black dashed line).

Figure S2: Layout of the microfluidic rapid-dilution device

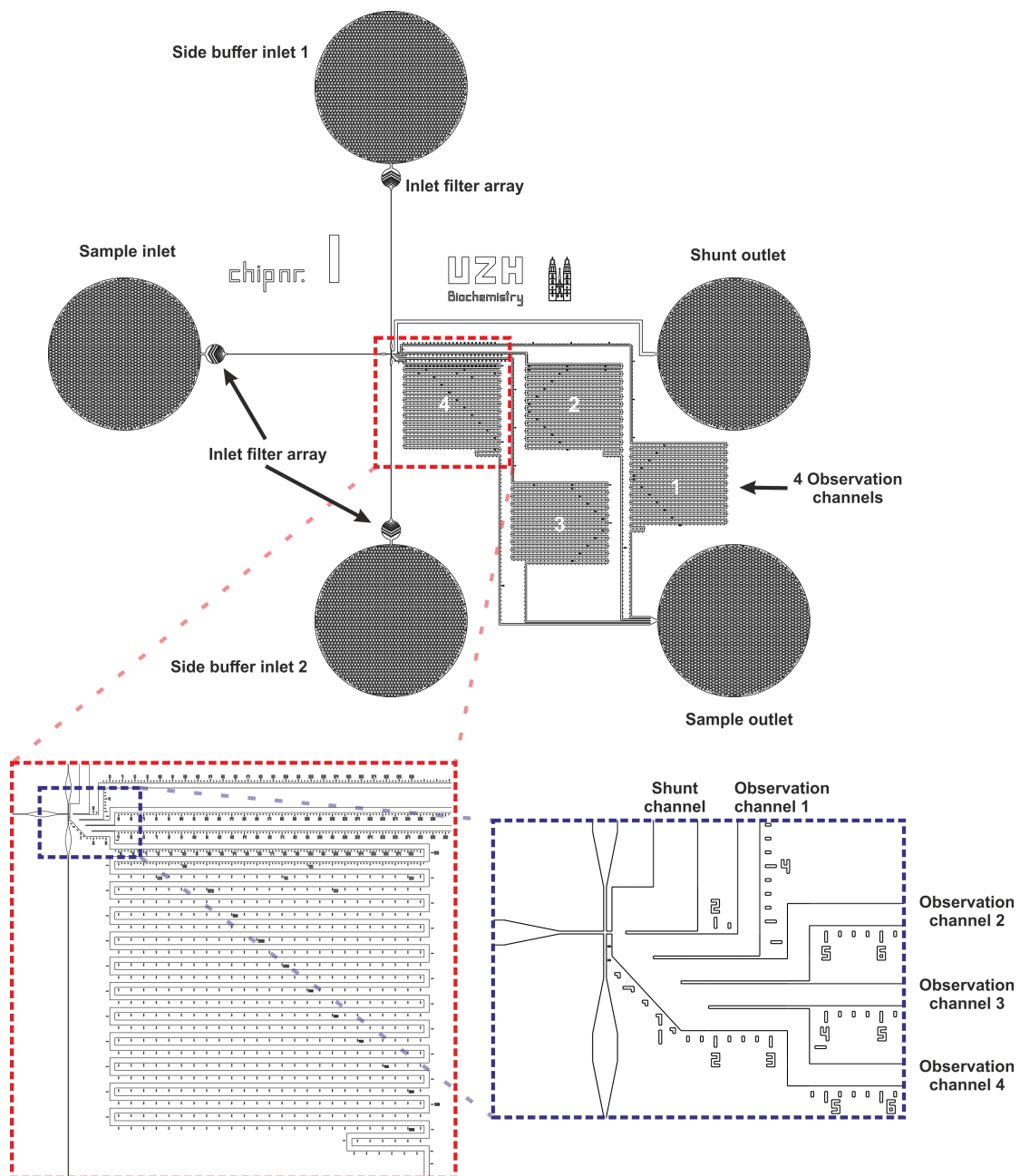


Figure S2: Overview showing the full layout of the device with increasing blow-ups of the dilution region. Sample solution from the center sample inlet is merged with buffer from the side inlets to create a hydrodynamically focused stream of sample molecules, corresponding to a steep concentration gradient. Subsequently, most of the sample is diverted to the shunt channel, while a minor part is shaved-off into the observation channels (see blue rectangle at bottom right). The microfluidic device includes four observation channels, thus offering a wide range of dilution factors. The 70 mm long observation channels are organized in a serpentine fashion (see red square at bottom left), enabling observation times of up to 3 minutes after dilution. The ticks and numbering are present throughout the device to facilitate exact positioning of the confocal volume. Filter arrays are incorporated in the inlet channels to prevent channel blockage by dust or particulate impurities in the sample.^[4]

Figure S3: SEM characterization of microfluidic device

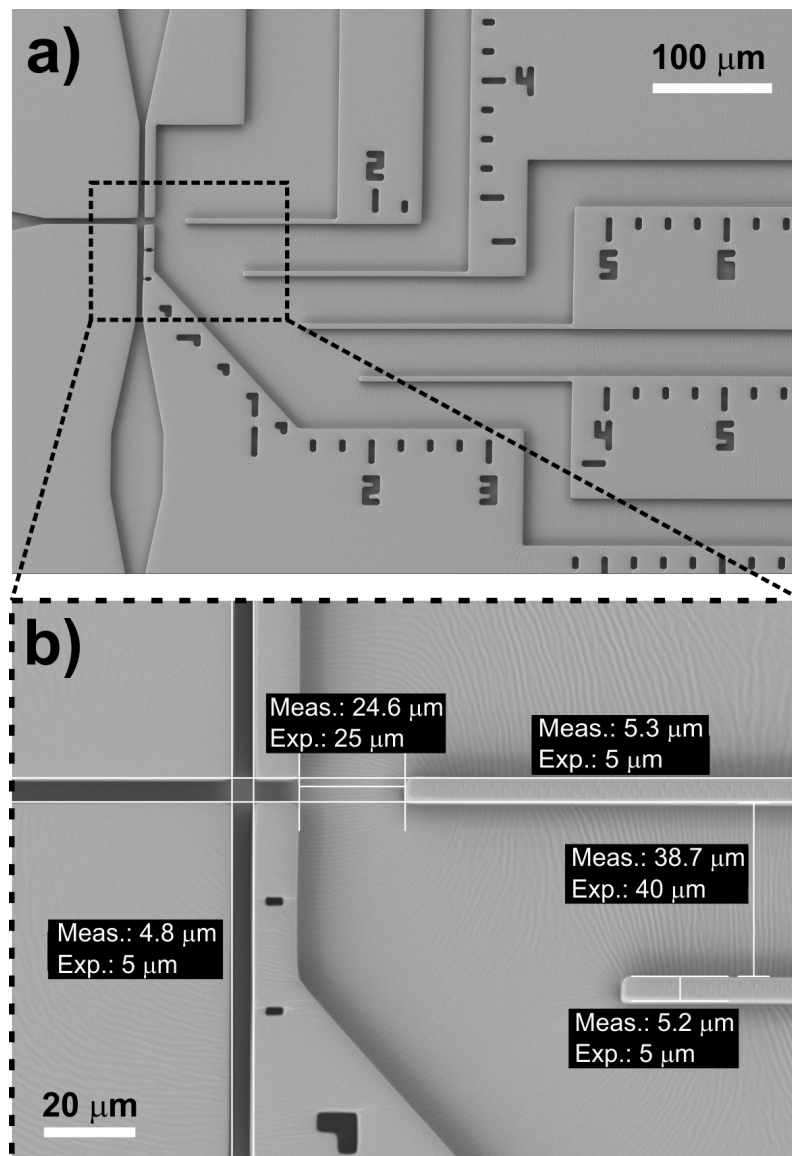


Figure S3: Scanning electron micrographs of the rapid dilution device showing the sample channel coming from the left and the buffer channels from top and bottom. **(a)** Overview of the sectioning wedges in the dilution region and the beginning of the four observation channels. **(b)** Zoom of the sectioning wedges with the feature sizes as measured in the scanning electron micrograph (Meas.) and the expected dimensions (Exp.), illustrating that the fabrication process is accurate within $\pm 5\%$.

Figure S4: Typical two-focus FCS curves

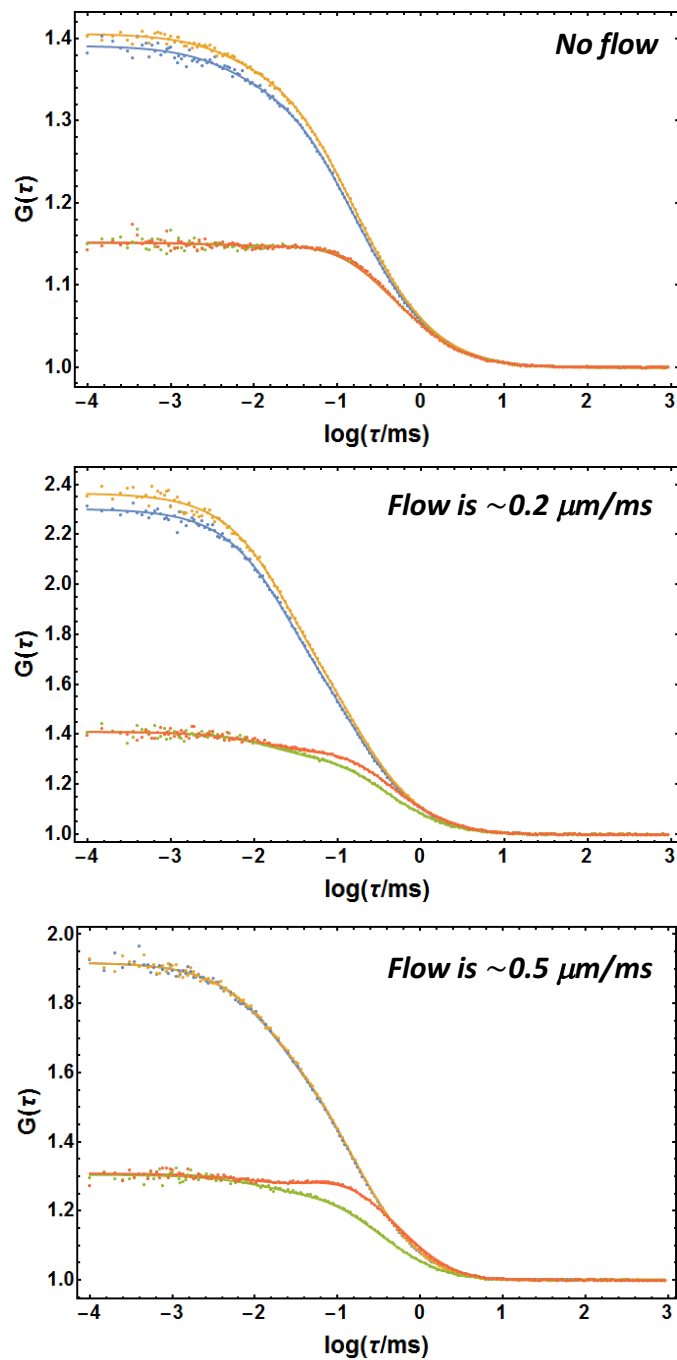


Figure S4: Typical fitted correlation curves obtained from two-focus FCS measurements used for characterizing the flow velocities in the microfluidic device. Each data set consists of four curves: two autocorrelations (one for each focus, blue and yellow) and the forward and reverse cross-correlations (between foci, orange and green, respectively). Note the characteristic difference between forward and reverse cross-correlations characteristic of flow.

Figure S5: Measured versus calculated flow velocities

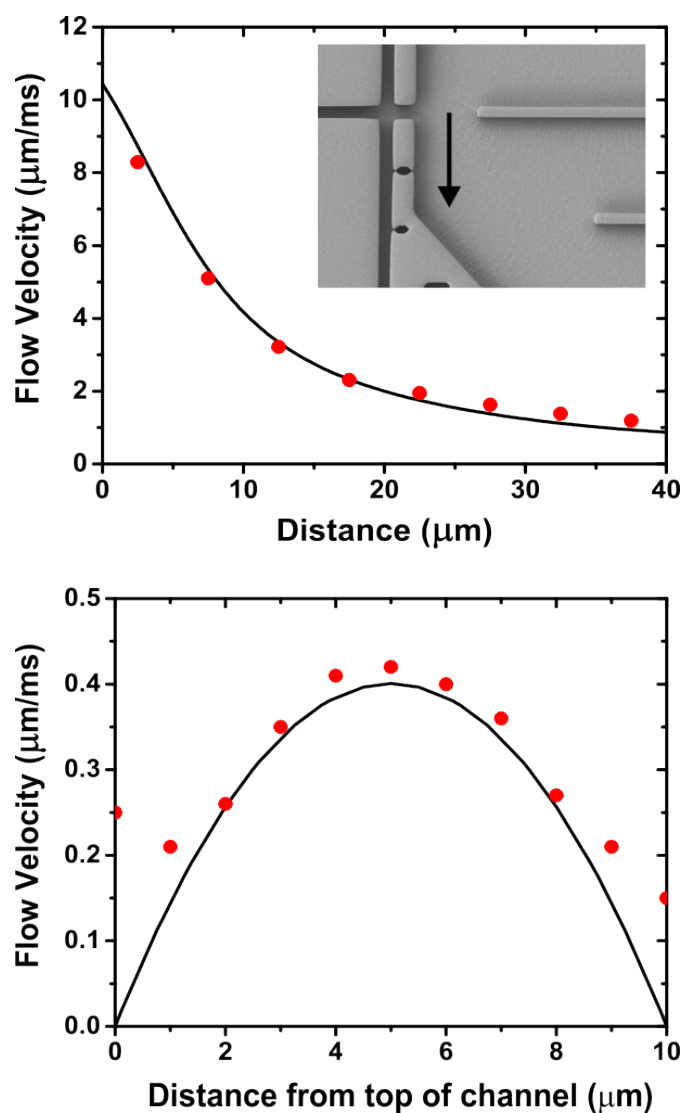


Figure S5: Flow velocities in the region of concentration sectioning (top figure) and across the second observation channel (bottom figure) were determined with two-focus FCS (red circles) and compared with the results from the finite-element calculations (black line). In both cases, the measured flow velocities are in good agreement with the calculated velocities. The deviations of the two-focus FCS data from the calculated velocities near the channel walls are most probably caused by distortions of the confocal volume at the PDMS/solvent interfaces.

Figure S6: Impulse response and position-to-time conversion

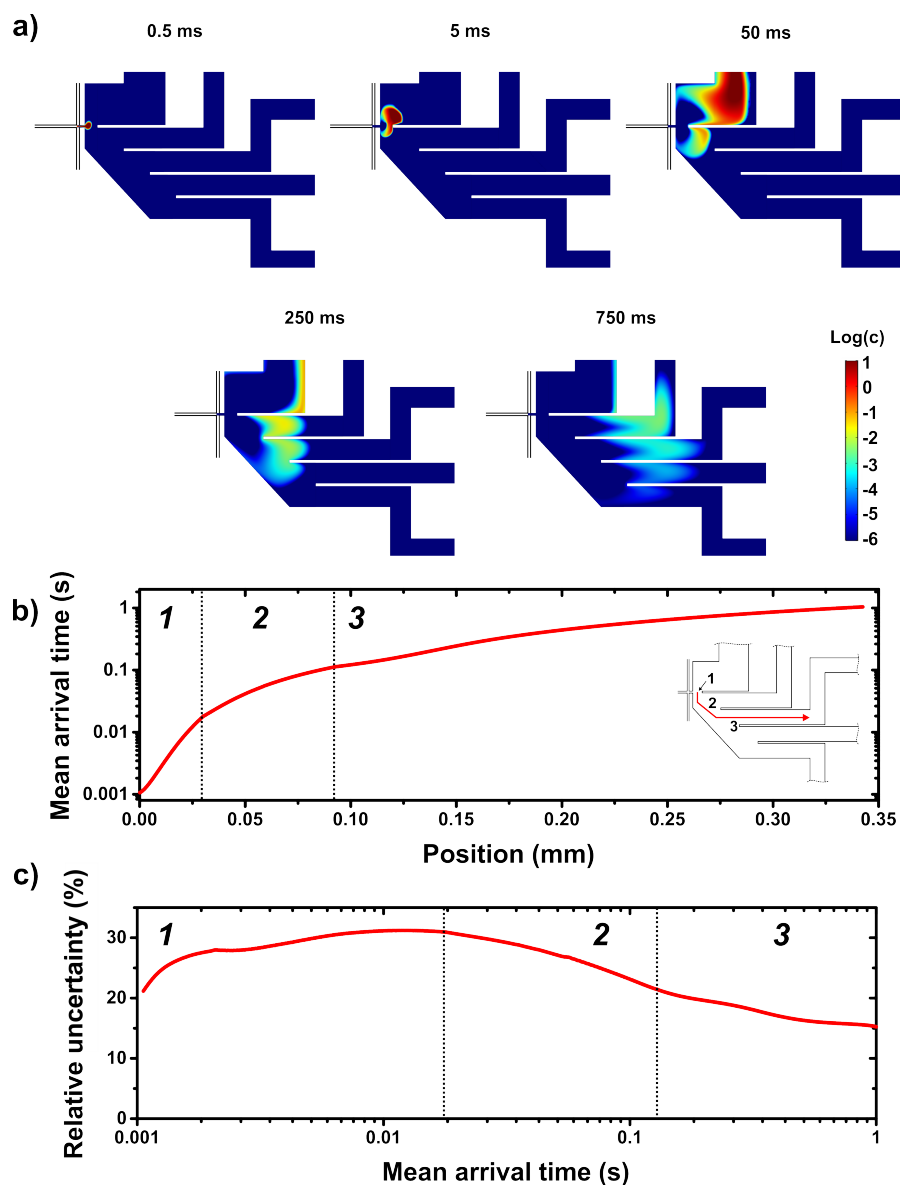


Figure S6: 3D time-resolved impulse response calculations used to convert positions within the microfluidic device to times after dilution. **(a)** Snapshots of the sample distribution in the device for different times after releasing a narrow pulse of sample at the point where the inlet channels meet. The color scaling indicates low sample concentrations in blue and high concentrations in red (shown on a logarithmic scale). For the full movie of the sample pulse traveling through the microfluidic device, see Supporting Video 1. **(b)** Mean arrival times of the sample molecules after dilution along the line indicated in the inset, corresponding to the streamline along which all measurements were taken here (Figures 2d- f, and Figures S7-S9). **(c)** The relative uncertainties of the arrival times (σ_{rel} , see Materials and Methods for details) along the same line versus the corresponding mean arrival times, illustrating the intrinsic uncertainty of arrival times due to Taylor dispersion.^[2-3]

Figure S7: Full series of two-color FRET efficiency histograms

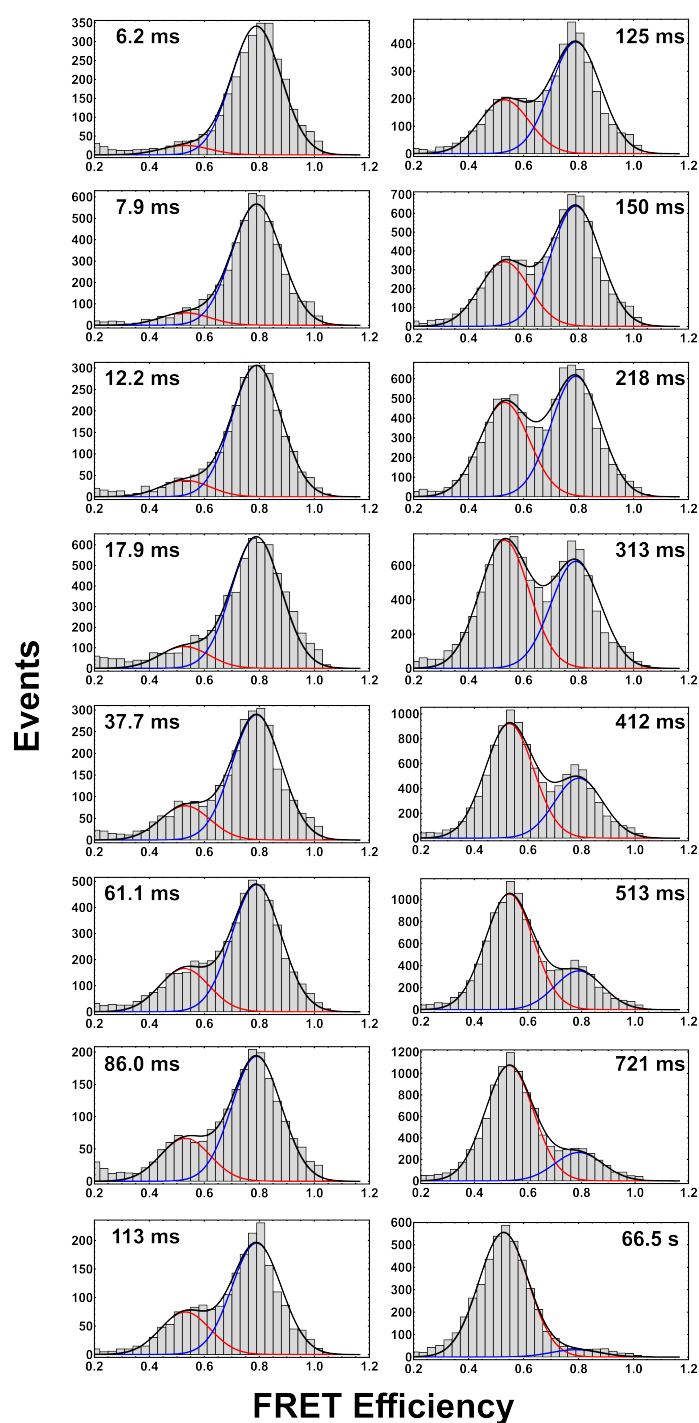


Figure S7: Full series of 2c-FRET efficiency histograms measured for the dissociation of the ACTR-NCBD complex, covering times after dilution from 6.2 ± 0.6 ms to 66.5 ± 3.3 s. The histograms show the two relevant peaks (the peak at zero transfer efficiency was removed using alternating excitation). The transfer efficiency peak at $E = 0.79$ corresponds to the protein complex and the peak at $E = 0.53$ to unbound ACTR. The histograms were fitted globally using a two-population model (black lines, individual populations are shown as red and blue lines, for details see Materials and Methods).

Figure S8: Experimental determination of the earliest observation time

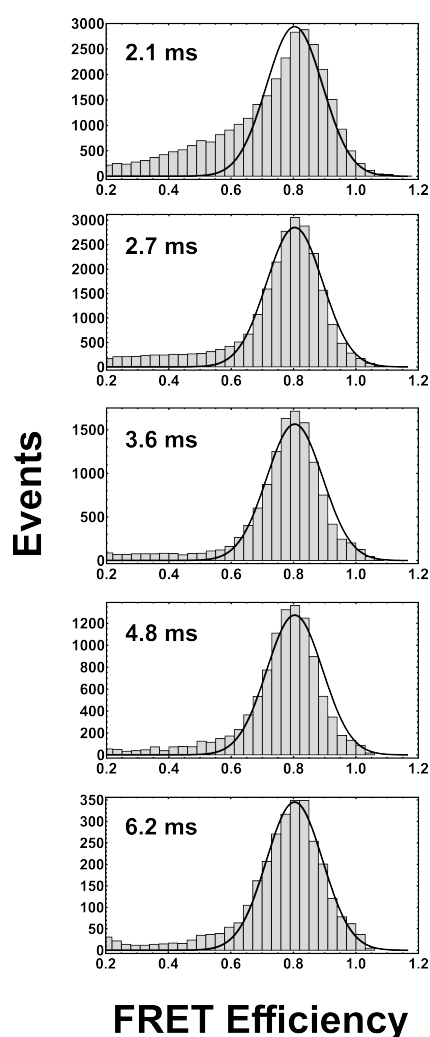


Figure S8: Transfer efficiency histograms measured for the ACTR-NCBD complex at different times after dilution. The sample inlet was loaded with preformed ACTR-NCBD complexes ($1 \mu\text{M}$ of labeled ACTR and $1.75 \mu\text{M}$ of NCBD, $\sim 99\%$ in complex). Since both buffer inlets were filled with $1.75 \mu\text{M}$ unlabeled NCBD, the NCBD concentration remained high throughout the microfluidic device, resulting in a high fraction of complex at all times. Therefore, only a single peak with high transfer efficiency corresponding to the protein complex is observed.

The transfer efficiency histograms show that the mean transfer efficiency of a single species can already be determined accurately at $2.7 \pm 0.3 \text{ ms}$ after dilution. Due to the low number of photons per burst (as a result of the high flow velocities) and the relatively high sample concentration in this region, an elevated background is visible at earlier times.

Both the flow velocity and the sample concentration continue to decrease until $\sim 5 \text{ ms}$ after dilution, and histograms suitable for accurately determining absolute ratios of populations can be recorded starting at $\sim 6 \text{ ms}$ after dilution, close to the dead time expected from diffusion-limited dilution for a 20,000-fold dilution (Figure S1). Solid lines show a fit to the data assuming a single species with identical transfer efficiency at all times.

Figure S9: Full series of 3c-FRET 2D histograms

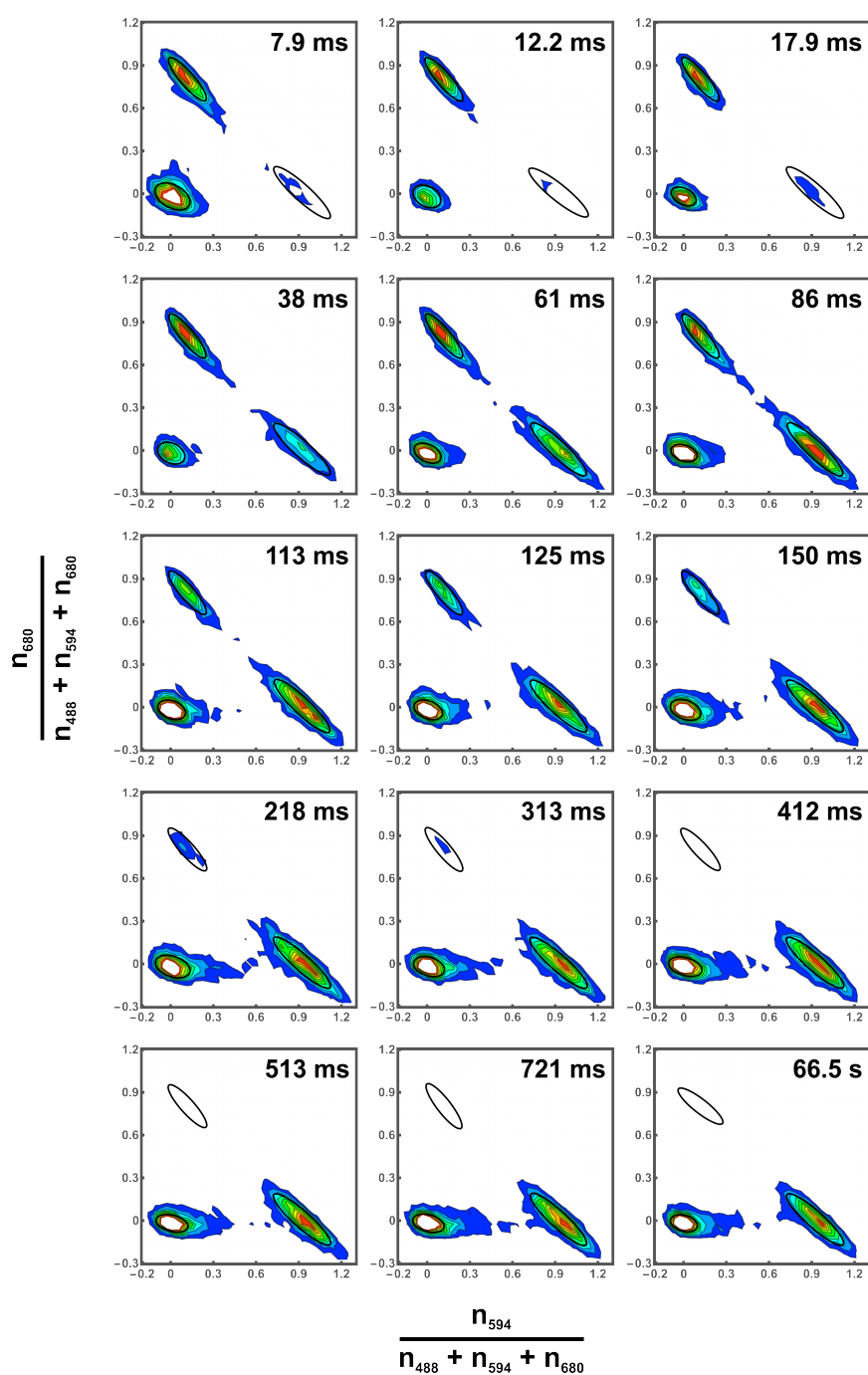


Figure S9: Full series of 2D histograms for the 3c-FRET experiments showing that the rapid dilution device can be used to probe the properties of a transiently populated protein complex. The histograms show the number of photons emitted by Alexa 594 (n_{594} , indicative of the unbound NCBP) versus the number of photons emitted by CF680R (n_{680} , indicative of the ACTR-NCBP complex), both are normalized to the total number of photons emitted by all three dyes. The black ellipses show the one standard deviation contour of the 2D Gaussian peak fits used to determine the fraction of complex (Figure S10). All histograms are normalized to the maximum of the bound or unbound population (whichever is greater).

Figure S10: Dissociation kinetics from 3c-FRET

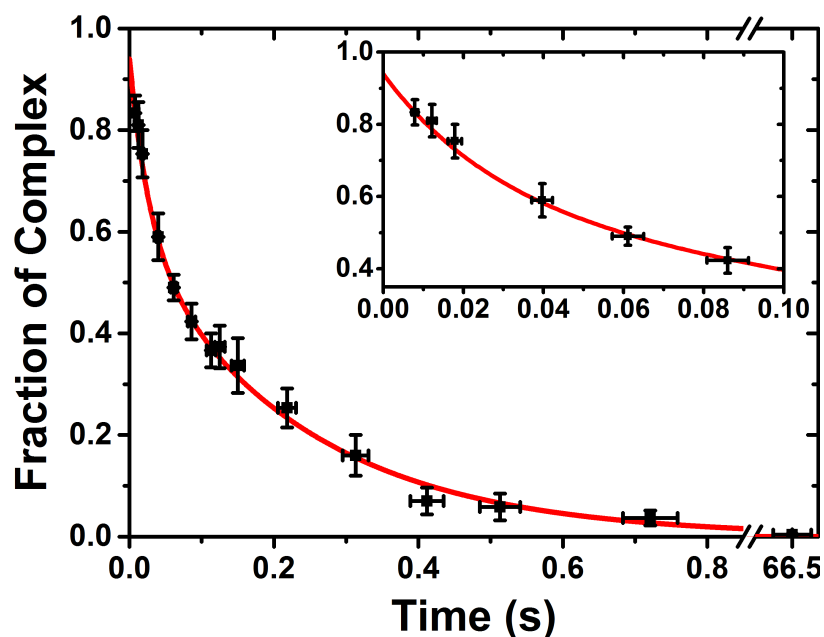


Figure S10: The fraction of complex (solid black circles) was determined from 2D Gaussian fits of the 3c-FRET 2D photon count ratio histograms (Figure S9) and plotted as a function of time after dilution. The error in the fraction of complexes is given by the standard deviation obtained from three independent measurements. The horizontal error bars were calculated assuming an uncertainty of $\pm 0.5 \mu\text{m}$ in position and $\pm 5\%$ flow velocity variations.^[4] The data were fitted with a double exponential decay (solid red line), where the initial fraction bound was fixed to 0.94, the value expected before dilution based on the K_d ($60 \pm 15 \text{ nM}$). The resulting dissociation rate constants were $k_{off,1} = 4.3 \pm 0.4 \text{ s}^{-1}$ and $k_{off,2} = 37 \pm 10 \text{ s}^{-1}$, in good agreement with the rates found in the 2c-FRET experiments, with small differences presumably resulting from differences in fluorescent labeling and buffer conditions.

Figure S11: Comparison of independent measurements in different microfluidic chips

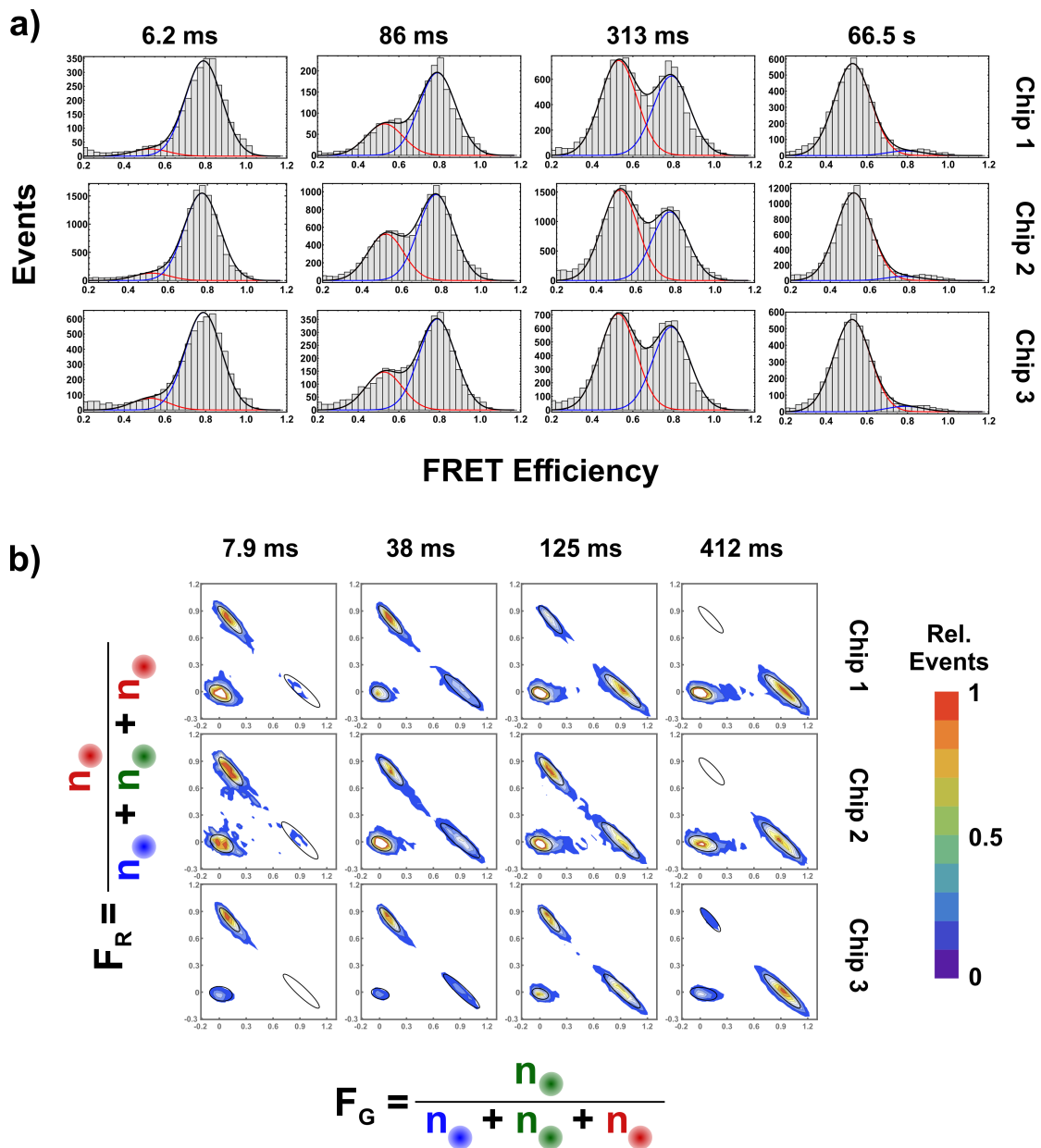


Figure S11: Comparison of the data obtained from three separate microfluidic devices at four different times after dilution for both the 2c-FRET (a) and 3c-FRET (b) measurements. The similarity of the histograms illustrates the reproducibility of data obtained from independent measurements in separate microfluidic devices.

Figure S12: Dissociation kinetics of destabilized ACTR-NCBD complex

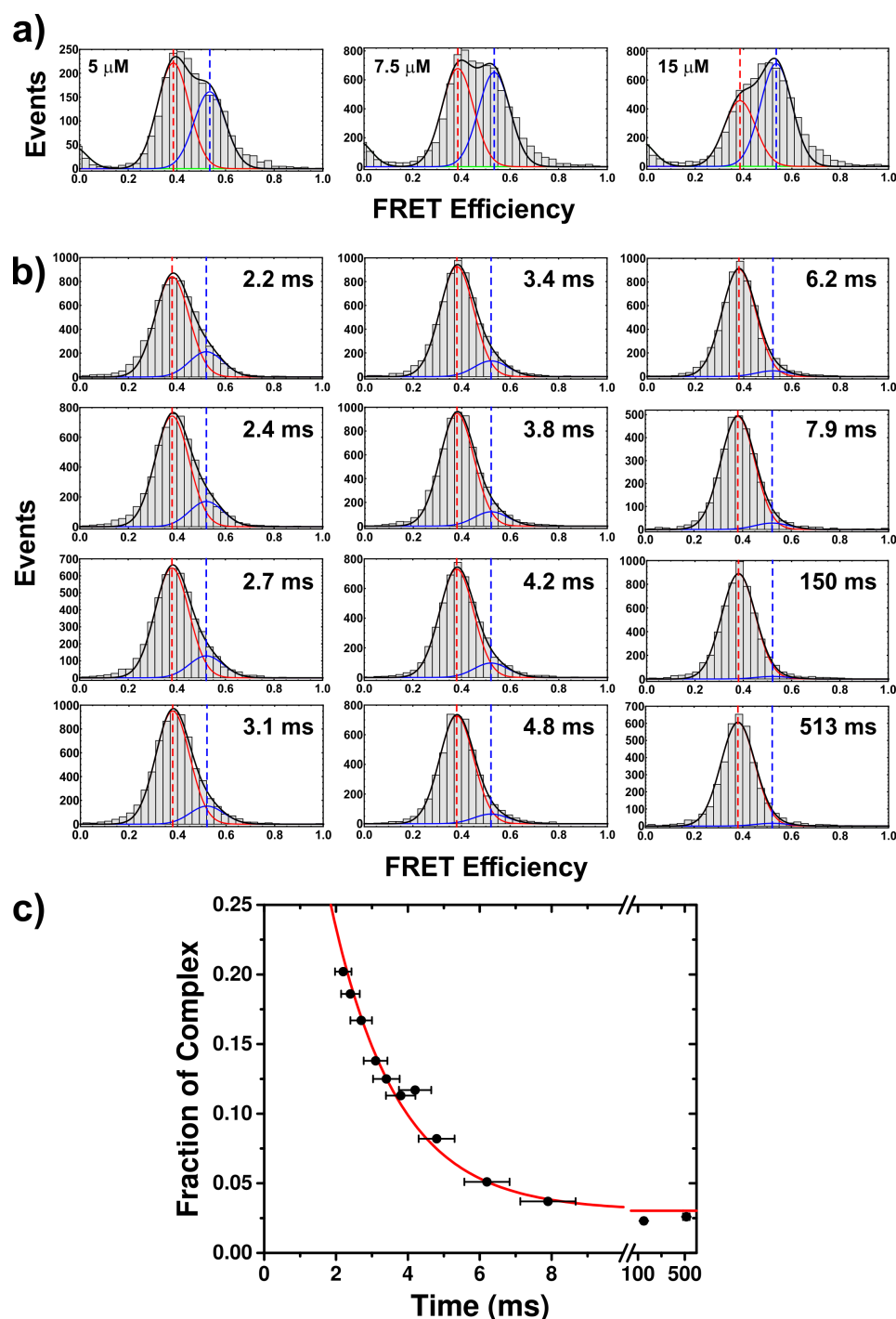


Figure S12: a) Examples of transfer efficiency histograms of the equilibrium titration measurements to determine the dissociation constant of the ACTR-NCBD complex, which was destabilized by adding 3 M Urea to the solutions. From these measurements, where 100 pM of donor- (Cy3B) and acceptor- (LD650) labeled ACTR was mixed with increasing concentrations of NCBD (5 – 15 μM , see graphs), a dissociation constant K_d of $\sim 8 \mu\text{M}$ was determined.

The transfer efficiency peak at $E = 0.52$ corresponds to the protein complex and the peak at $E = 0.38$ to unbound ACTR. The shift of the transfer efficiency to lower values as compared to the previous 2c-FRET measurements is due to the denaturing effect of Urea

which results in an expansion of both the free ACTR protein^[14] and the ACTR-NCBD complex. The histograms were fitted globally using a two-population model (black lines; individual populations are shown as red and blue lines; for details see Materials and Methods). The blue and red dashed lines indicate the peak positions of both species.

b) Full series of 2c-FRET efficiency histograms of the dissociation of the destabilized ACTR-NCBD complex measured in the microfluidic device, covering times after dilution from 2.2 ± 0.4 ms to 513 ± 28 ms.

c) The fraction of complex (black circles) determined from the fits to the transfer efficiency histograms as a function of time after dilution. The horizontal error bars were obtained assuming an uncertainty of ± 0.5 μm in position and flow velocity variations of $\pm 5\%$.^[4] The data were fitted with a single-exponential decay (solid red line), with the initial fraction bound fixed to 0.60, the value expected before dilution based on the K_d (~ 8 μM) and the starting concentrations of ACTR and NCBD (see Materials and Methods). The resulting dissociation rate constant was $k_{off} = 540 \pm 21$ s^{-1} .

Figure S13: Dilution factors for a range of diffusion coefficients from finite-element calculations

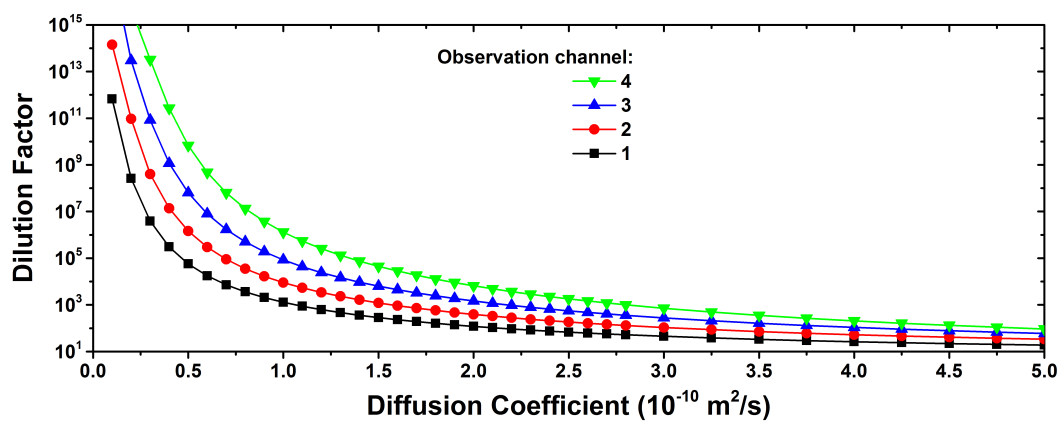


Figure S13: Calculated dilution factor for each of the four observation channels for a range of diffusion coefficients of the sample from finite-element calculations. The dilution factor depends on the diffusion coefficient of the sample, since it determines how quickly the protein molecules will distribute across the narrow channel following the region of hydrodynamic focusing. The faster this diffusive mixing occurs, the lower the dilution factor.

Figure S14: FCS calibration measurements

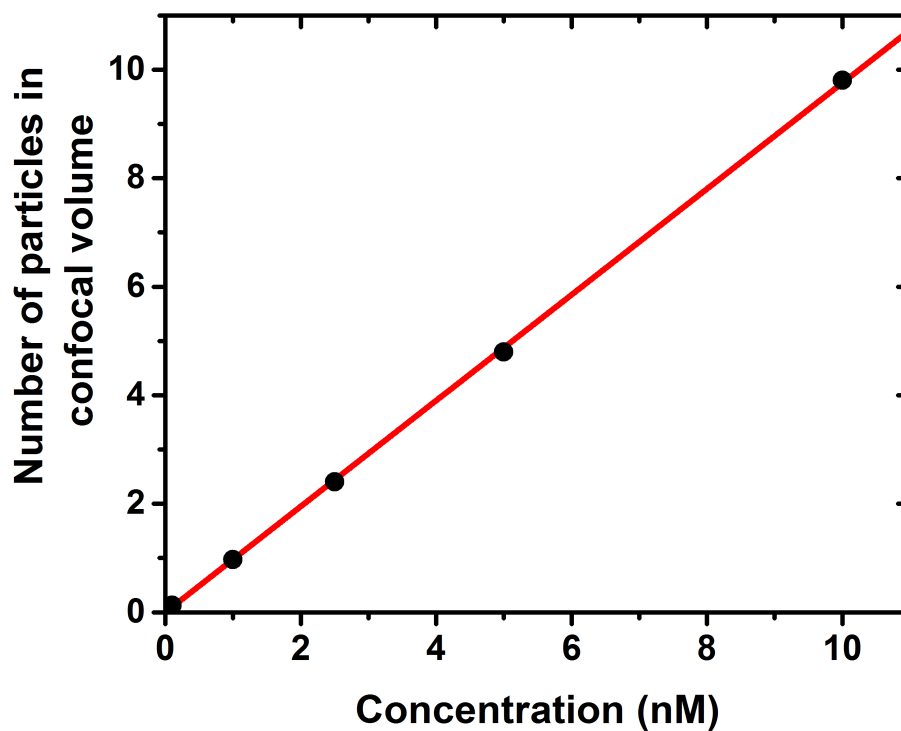


Figure S14: Calibration measurements for fluorescence correlation spectroscopy (FCS) using ACTR fluorescently labeled with Atto532. Based on this calibration, the average number of particles in the confocal volume observed in the microfluidic device can be converted to a concentration, and hence to a dilution factor, since the initial concentration is known.

Figure S15: Typical intensity time traces for single-molecule 2c-FRET measurements

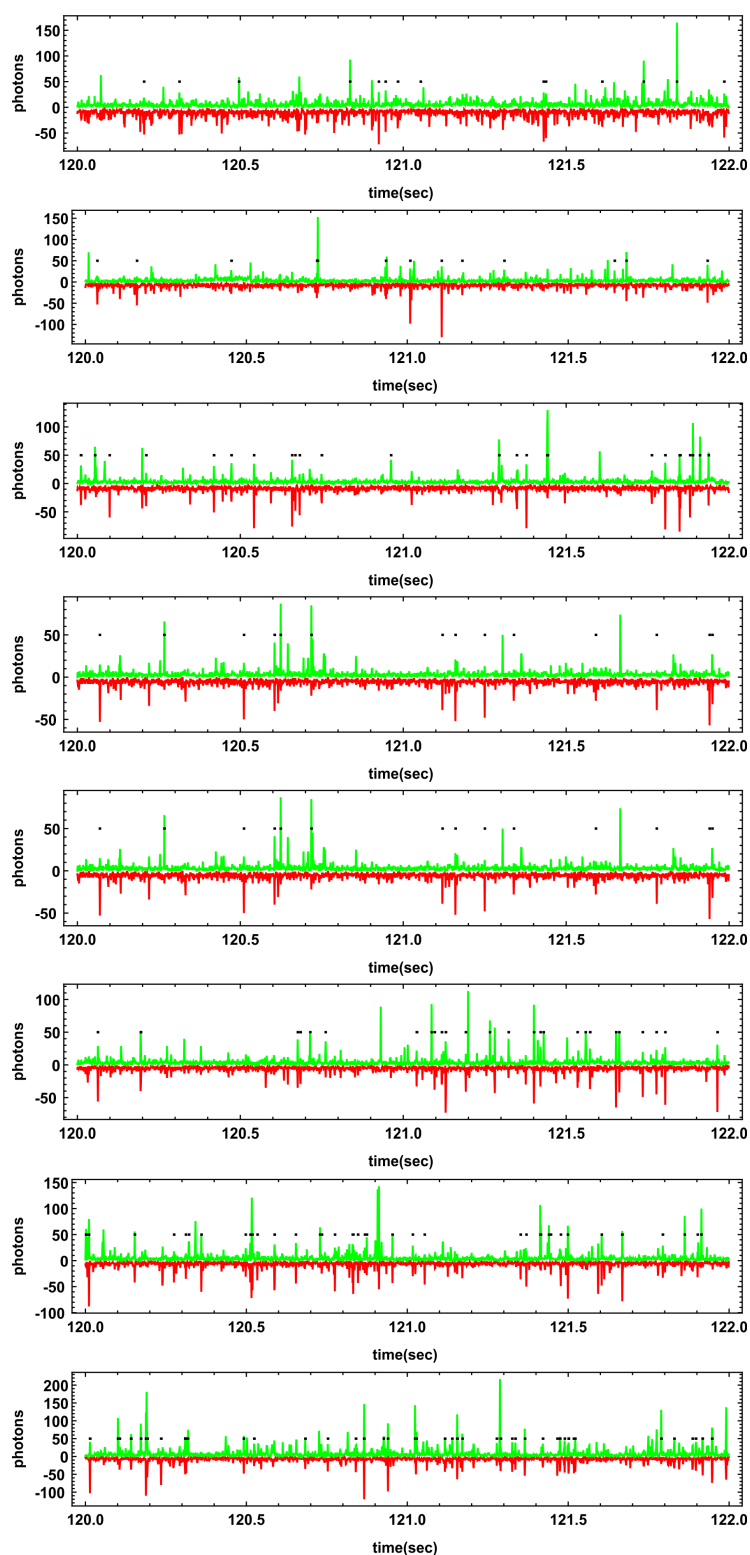


Figure S15: Parts of typical intensity time traces obtained from the 2c-FRET measurements. The donor photons are shown in green and the acceptor photons in red (1 ms time binning shown). The black dots in each intensity time trace indicate the fluorescence burst identified using the criteria described in the Materials & Methods section and used for the subsequent data analysis.

References

- [1] T. J. Arbour, J. Enderlein, *Lab Chip* **2010**, *10*, 1286-1292.
- [2] B. Wunderlich, D. Nettels, B. Schuler, *Lab Chip* **2014**, *14*, 219-228.
- [3] G. Taylor, *Proc. R. Soc. London, A* **1953**, *219*, 186-203.
- [4] B. Wunderlich, D. Nettels, S. Benke, J. Clark, S. Weidner, H. Hofmann, S. H. Pfeil, B. Schuler, *Nat. Protocols* **2013**, *8*, 1459-1474.
- [5] J. Schilling, J. Schöppe, A. Plückthun, *J. Mol. Biol.* **2014**, *426*, 691-721.
- [6] M. G. Cull, P. J. Schatz, in *Methods Enzymol., Vol. Volume 326*, Academic Press, **2000**, pp. 430-440.
- [7] R. B. Altman, D. S. Terry, Z. Zhou, Q. Zheng, P. Geggier, R. A. Kolster, Y. Zhao, J. A. Javitch, J. D. Warren, S. C. Blanchard, *Nat. Methods* **2012**, *9*, 68-71.
- [8] A. Soranno, I. Koenig, M. B. Borgia, H. Hofmann, F. Zosel, D. Nettels, B. Schuler, *Proc. Natl. Acad. Sci. U. S. A.* **2014**, *111*, 4874-4879.
- [9] D. Magde, W. W. Webb, E. L. Elson, *Biopolymers* **1978**, *17*, 361-376.
- [10] B. K. Müller, E. Zaychikov, C. Bräuchle, D. C. Lamb, *Biophys. J.* **2005**, *89*, 3508-3522.
- [11] C. Eggeling, S. Berger, L. Brand, J. R. Fries, J. Schaffer, A. Volkmer, C. A. M. Seidel, *J. Biotechnol.* **2001**, *86*, 163-180.
- [12] F. Hillger, D. Hänni, D. Nettels, S. Geister, M. Grandin, M. Textor, B. Schuler, *Angew. Chem., Int. Ed.* **2008**, *47*, 6184-6188.
- [13] A. N. Kapanidis, N. K. Lee, T. A. Laurence, S. Doose, E. Margeat, S. Weiss, *Proc. Natl. Acad. Sci. U. S. A.* **2004**, *101*, 8936-8941.
- [14] A. Borgia, W. Zheng, K. Buholzer, M. B. Borgia, A. Schüler, H. Hofmann, A. Soranno, D. Nettels, K. Gast, A. Grishaev, R. B. Best, B. Schuler, *J. Am. Chem. Soc.* **2016**, *138*, 11714-11726.